This paper is a peer-reviewed pre-print submitted to EarthArXiv. The manuscript has been accepted at Geochemistry, Geophysics, Geosystems and is available at https://doi.org/10.1029/2023GC011357.

Plagioclase-saturated melt hygrothermobarometry and plagioclase-melt equilibria using machine learning

K. S. Cutler[1*], M. Cassidy[1,2], and J.D. Blundy[1]

1 Department of Earth Sciences, University of Oxford, South Parks Road, Oxford, OX1 3AN, UK

2 School of Geography, Earth and Environmental Sciences, University of Birmingham, Edgbaston, Birmingham, B15 2TT, UK

Corresponding author: Kyra Cutler (kyra.cutler@stx.ox.ac.uk)

Key Points:

- Investigation into whether existing plagioclase-based hygrothermobarometers can be refined using random forest machine learning.
- The algorithm highlights that only melt composition is required to estimate intensive variables (P-T-H_2O) of plagioclase-saturated magmas.
- New melt models show improvement in errors compared to thermodynamic-based plagioclase-melt hygrothermobarometers and equilibria models.

Abstract

Compositions of plagioclase-melt pairs are commonly used to constrain temperatures (T), dissolved water contents (H_2O) and pressures (P) of pre-eruptive magma storage and transport. However, previous plagioclase-based thermometers, hygrometers, and barometers can have significant errors, leading to imprecise reconstructions of conditions during plagioclase growth. Here, we explore whether we can refine existing plagioclase-based hygrothermobarometers with either plagioclase-melt or melt-only chemistry (± T/H_2O), calibrated using random forest machine learning on experimental petrology data (n= 1152). We find that both the plagioclase-melt and melt-only models return similar cross-validation root-mean-square errors (RMSEs), as the melt holds most of the P-T-H_2O information rather than the plagioclase. T/H_2O-dependent melt models have test set RMSEs of 25 °C, 0.70 wt.% and 76 MPa for temperature, H_2O content and pressure, respectively, while T/H_2O-independent models have RMSEs of 38 °C, 0.97 wt.% and 91 MPa. The melt thermometer and hygrometer are applicable to a wide range of plagioclase-bearing melts at temperatures between 664 and 1355 °C, and with H_2O concentrations up to 11.2 wt.%, while the melt barometer is suitable for pressures of ≤500 MPa. An updated plagioclase-melt equilibrium model has also been calibrated, allowing equilibrium anorthite content to be predicted with an error of 5.8 mol%. The new P-T-H_2O-An models were applied to matrix glasses and melt inclusions from the 1980 Mount St Helens (USA) and 2014-2015 Holuhraun (Iceland) eruptions, corroborating previous independent estimates and observations. Models are available at: https://github.com/kyra-cutler/Plag-saturated-melt-P-T-H2O-An, enabling assessment of plagioclase-melt equilibrium and characterisation of last-equilibrated P-T-H_2O conditions of plagioclase-saturated magmas.

Plain Language Summary

Thermobarometry and hygrometry are common methods for reconstructing magma crystallisation conditions (pressure (P), temperature (T) and dissolved water contents (H_2O)) prior to eruption. Plagioclase is a ubiquitous mineral found in a wide range of volcanic rocks and is often used to estimate P-T-H_2O conditions. Here, we use machine

learning-based regression to calibrate new models, based on either plagioclase-melt or melt-only chemistry, to test whether we can improve the existing range of plagioclase-based thermobarometers and hygrometers. We also develop an updated model to determine the equilibrium composition of a plagioclase crystal with a given normalised melt composition. We find that the plagioclase-melt and melt-only thermobarometers and hygrometers return very similar model errors due to the melt holding nearly all the P-T-H_2O information. The models can be applied to a wide range of plagioclase-bearing melts except for the barometer, which is only appropriate for upper crustal pressures of ≤500 MPa (≤13.8 km depth). Models are available to use at: https://github.com/kyra-cutler/Plag-saturated-melt-P-T-H2O-An, enabling assessment of plagioclase-melt equilibrium and characterisation of last-equilibrated P-T-H_2O conditions of plagioclase-saturated magmas.

1 Introduction

Temperature (T), pressure (P) and melt water contents (H_2O) collectively control various physiochemical properties of magmas by influencing the crystallisation and stability of mineral phases (e.g., Feig et al., 2010; Krawczynski et al., 2012), as well as the density and viscosity of melts (e.g., Giordano et al., 2008). Placing constraints on the thermal state, volatile concentration, and depths of magma crystallisation thereby enables a critical insight into pre-eruptive storage conditions and magma transport properties, informing our understanding of controls on eruption dynamics and the crustal architecture of sub-volcanic systems (e.g., Cassidy et al., 2018; Bamber et al., 2022; Caricchi et al., 2021; Giordano and Caricchi, 2022). Furthermore, integrating petrological constraints with potential signs of volcanic unrest (i.e., seismicity, surface deformation, gas emissions; e.g., Saunders et al., 2012; Stock et al., 2018; Cassidy et al., 2019; Liu et al., 2020; Yip et al., 2022) can facilitate monitoring and hazard management at restless volcanoes (e.g., Pritchard et al., 2019).

Plagioclase is an abundant mineral found in volcanic rocks across a wide compositional range, with its chemistry sensitive to temperature, melt composition – including water content – and pressure (e.g., Housh and Luhr, 1991; Longhi et al., 1993;

Panjasawatong et al., 1995; Lange et al., 2009; Namur et al., 2012). This has led to the development of a range of plagioclase-melt thermometers, hygrometers and barometers (e.g., Putirka, 2005; Putirka, 2008; Lange et al., 2009; Waters and Lange, 2015; Masotta and Mollo, 2019), with expressions based on the equilibrium exchange of albite (Ab; $NaAlSi_3O_8$) and anorthite (An; $CaAl_2Si_2O_8$) components between plagioclase and melt (Equation 1):

$$CaAl_2Si_2O_8^{crystal} + NaAlSi_3O_8^{melt} = CaAl_2Si_2O_8^{melt} + NaAlSi_3O_8^{crystal} \quad (1)$$

Temperature and melt water contents recovered with plagioclase-melt thermometers and hygrometers have relatively small errors (e.g., Equation 24a, ± 36 °C; Putirka, 2008; ± 0.29 wt.% (trachyte-specific) Masotta and Mollo, 2019; 0.35 wt.%, Waters and Lange, 2015; 1.1 wt.%, Putirka, 2008 (Equation 25b)), although such models are dependent on at least one independently-constrained intensive variable (i.e., T, H_2O or P), yielding higher errors when errors are propagated or iterative calculations are performed (Wieser et al., 2023a). The only plagioclase-melt barometer available is a formulation by Putirka (2005, 2008), which returns a significantly large Standard Error Estimate (SEE: 380 MPa; which is equivalent to ± 10.5 km depth uncertainty using a 2700 kg/m^3 crustal density), resulting from the negligible volume change of reaction (Equation 1) at low pressures (c.f. ≤300 MPa; Lange et al., 2009). Similarly, other mineral-based barometer calibrations are associated with comparably poor accuracy and precision (e.g., clinopyroxene: 200–500 MPa, ± 5.5–14 km depth, Wieser et al., 2023b; amphibole: 300–400 MPa, ± 8–11 km, Putirka, 2016), sufficient only for outlining broad depth ranges of magma crystallisation. Establishing a precise and accurate barometer is thus a key petrological target for obtaining high-resolution images of magmatic systems, as identified by the SZ4 initiative (Hilley et al., 2022). The poor performance prevalent in the current scope of barometers may derive from various factors, including low precision electron microprobe measurements on pressure-sensitive analytes (i.e., Na_2O in clinopyroxene; Wieser et al., 2023a), disequilibrium textures in experimental products (e.g., clinopyroxene sector zoning; Neave et al., 2019), or a weak pressure dependency on compositional variables (e.g., Putirka, 2016). Another factor that can contribute to the large uncertainty of pressure estimates is the strategy used to calibrate barometric models (Higgins et al., 2022). Recently,

supervised machine learning (ML) algorithms have proven to be a successful approach to obtain T and P predictions (e.g., Petrelli et al., 2020; Higgins et al., 2022; Thomson et al., 2021; Jorgenson et al., 2022), as the algorithms are not reliant on any a priori thermodynamic knowledge and can capture non-linearity between variables.

Over the past 50 years, several empirical or thermodynamic-based models have been developed to predict the equilibrium compositions of plagioclase (An = [molar Ca/(Ca + Na + K)]) crystallising from silicate melts. Although the majority of plagioclase-melt equilibria models primarily examine the effect of H_2O and pressure on plagioclase composition (e.g., Panjasawatong et al., 1995; Housh and Luhr, 1991), limited studies have focussed on anhydrous systems or combined (hydrous and anhydrous) datasets (e.g., Fuhrman and Lindsley, 1988; Namur et al., 2012; Putirka, 2005). This necessitates creating an updated plagioclase-melt equilibria model, applicable to modelling an extensive range of differentiated liquids irrespective of melt water content.

In this study, our aims are two-fold. With the large number of plagioclase-bearing experiments available, we first use machine learning (ML) to test whether we can refine the existing range (i.e., Putirka, 2005; Putirka, 2008; Waters and Lange, 2015; Masotta and Mollo, 2019) of plagioclase-based hygrothermobarometers, either by using plagioclase-melt or melt-only chemistry. Secondly, we aim to create an ML model for predicting equilibrium plagioclase compositions solely as a function of melt chemistry. We then test the capability of the models to recover magma crystallisation conditions at two well-studied volcanic systems, comparing P-T-H_2O-An estimates with melt inclusion analyses, geophysical data, and independent hygrothermobarometric and plagioclase-melt equilibria calculations.

2 Developing hygrothermobarometric and anorthite content models

2.1 Dataset compilation and filtering

Experimental plagioclase-melt pairs were extracted from the Library of Experimental Phase Relations (LEPR) database (Hirschmann et al., 2008) and supplemented by an extensive literature search to calibrate all plagioclase-melt and melt-only versions of models. The final dataset (n=1152) includes anhydrous/nominally

anhydrous, fluid-saturated and fluid-undersaturated experiments; the full calibration dataset can be accessed in Table S1. We applied a set of filters to the experimental data to ensure coexisting plagioclase-melt pairs were in equilibrium (e.g., Lange et al., 2009; Namur et al., 2012; Waters and Lange, 2015): (1) only experiments with a quenched liquid (i.e. glass) fraction of ≥50% were selected, as high crystallinity charges are subject to slower diffusion rates in minerals compared to the melt, requiring longer timescales to reach equilibrium. Experiments were excluded if phase or crystallinity proportions were not reported. (2) Only experiments with electron microprobe analytical totals between 97 and 101.5 wt.% (including H_2O) were incorporated. This filter ensures that any potential analytical errors are minimised. (3) Experiments were removed if papers reported evidence for significant sodium and/or iron loss (≥10 wt.% relative Na_2O or FeOt). It must be noted that some plagioclase-saturated melt compositions in the literature lack compositions of coexisting plagioclases. For the hygrometry models, only experiments with well-constrained water analyses (i.e., Fourier-Transform InfraRed spectroscopy, Secondary Ion Mass Spectroscopy, Raman spectroscopy) were used as the water content values for calibration. However, only ~35% of hydrous experiments have measured water content estimates. Therefore, MagmaSat (Ghiorso and Gualda, 2015) in VESIcal (Iacovino et al. 2021) was used to calculate the water content in the remaining water-saturated and undersaturated (if fluid XH_2O value was reported) experiments.

2.2. Calibration range

The calibration dataset covers a range of terrestrial and non-terrestrial analogue melts (SiO_2: 37.1–79.9 wt.%; $Na_2O + K_2O$: 0.3–14.6 wt.%) that crystallised plagioclase (An_{16-100}) at conditions from 0–2000 MPa, 664–1355 °C, and H_2O concentrations up to 11.2 wt.% (Figure 1). Temperature displays a bimodal distribution with peaks at 850–900 °C (felsic melts) and 1100–1200 °C (mafic melts), whereas plagioclase compositions are symmetrically distributed. Pressure and H_2O have strong positively-skewed distributions. Excluding the experiments undertaken at 1 atm, 85% of the experiments occur at pressures of ≤500 MPa. There is minimal variation in T and H_2O at pressures >500 MPa within the overall P range, except for the 700 MPa experiments

(Figure 1b). From all the hydrous experimental data, there is an evident lack of experiments with higher H_2O (>7 wt.%) contents, although 9 ± 1 wt.% represents the maximum limit to which H_2O in experimental mafic melts can be quenched to glass (Gavrilenko et al., 2019). Experiments with lower H_2O (<2 wt.%) are also underrepresented, reflecting limited studies that measure water content in near-anhydrous experimental glasses (i.e., Whittaker et al., 2007; Husen et al., 2016) and/or undertaking water-saturated runs at low pressures.

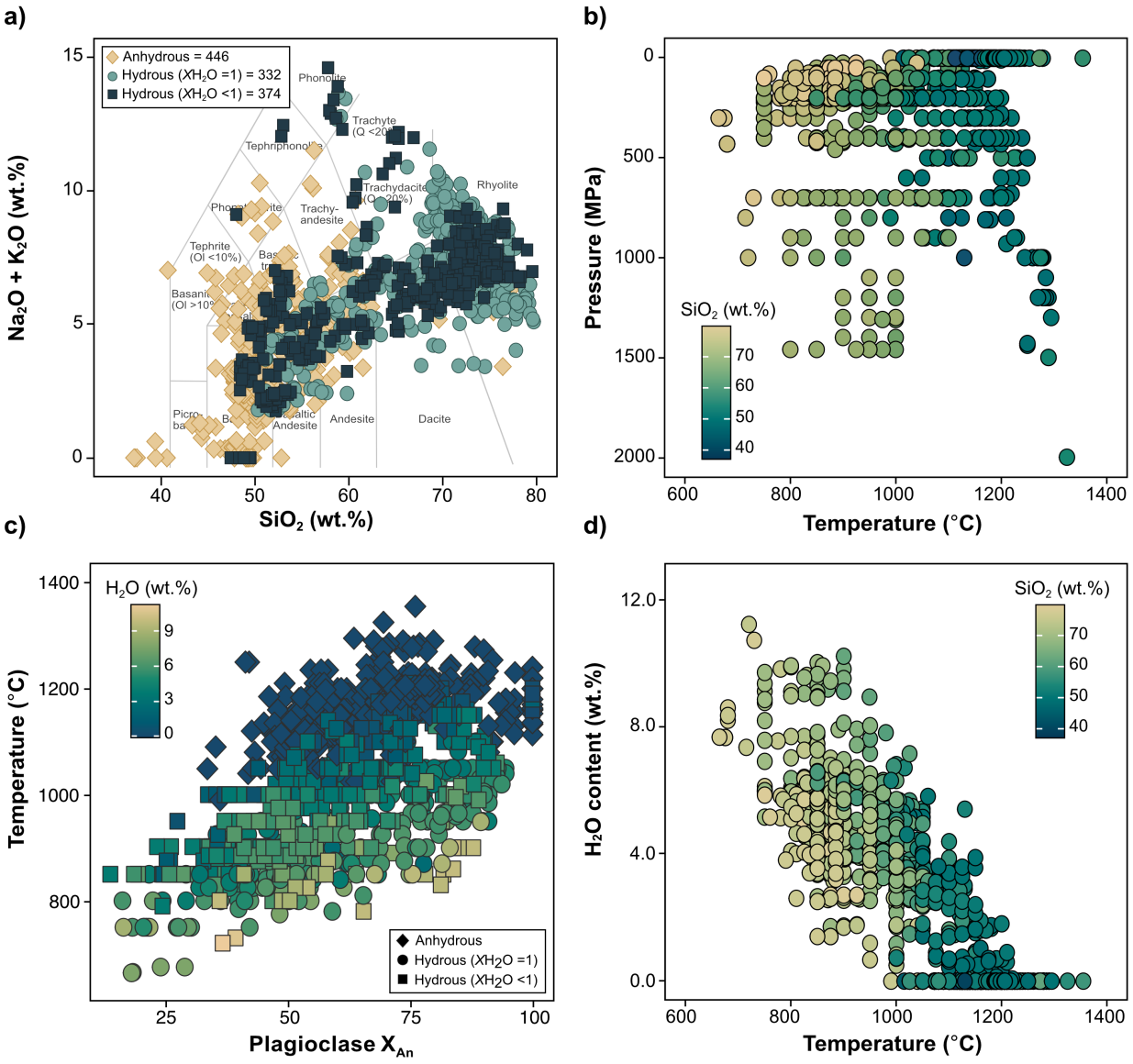

Figure 1. Calibration range of compiled plagioclase-saturated experiments. **a**) Total alkali silica classification diagram after Le Maitre et al. (1989) of experimental glass compositions (*n*=1152). The anhydrous experimental total includes nominally anhydrous experiments (*n*=17). **b**) Temperature (°C) versus pressure (MPa) of experiments. Colour coding indicates SiO_2 (wt.%) of the melt. **c**) Plagioclase composition in terms of temperature for all experimental data with plagioclase-melt compositions (*n*=1063) with colour coding highlighting melt H_2O (wt.%) content. **d**) H_2O

(wt.%) versus temperature (°C) of experiments. Colour coding reflects SiO_2 (wt.%) of the melt.

2.3. Model training and cross-validation

A type of random forest machine learning algorithm, Extremely Randomised Trees, was used to train all the models using the package 'ranger' and the *splitrule* 'extratrees' (Wright and Ziegler, 2017) in R (R Core Team, 2013), as it has been shown to have the highest predictive capability among a selection of supervised learning algorithms (e.g. Petrelli et al., 2020, Li and Zhang, 2022). In short, random forest algorithms are an ensemble machine learning approach involving multiple decision trees, where the output of all individual trees is aggregated to form an averaged prediction. Each target variable (P-T-H_2O-An) is predicted using normalised major element oxide compositions as dependent variables (melt: SiO_2, TiO_2, Al_2O_3, FeO_t, MgO, CaO, Na_2O, K_2O; plagioclase: SiO_2, Al_2O_3, FeO_t, CaO, Na_2O, K_2O) for the plagioclase-melt or melt-only models. MnO in the melt and MnO, TiO_2 and MgO in plagioclase were not considered as input variables since numerous experiments do not report one or more of these oxides and since they are uniformly at very low concentrations in plagioclase. The whole dataset was split into training and testing sets using an 80/20 ratio, with the test set held back and never used during model calibration. The training/testing sets were split using a stratified sampling function to ensure a balanced distribution of the models' target variable (i.e. H_2O, temperature, pressure and An content) in both the training and testing sets. Models can be optimised by tuning hyperparameters, but studies have shown that it has little impact on model performance (e.g., Petrelli et al., 2020; Jorgenson et al., 2022). Therefore, we used the default hyperparameter tuning (i.e., *mtry*) within the Caret package (Kuhn, 2008) to optimise each model while keeping the number of the decision trees small (*num.trees* = 200) to minimise computational time. We use the median to average the final prediction from the 200 individual decision trees (Figure S1a), which has been shown to return slightly lower RMSEs (Root Mean Square Errors) than the mean (Jorgenson et al., 2022; Weber and Blundy, 2024).

Model errors were assessed using two approaches. First, stratified 10-fold cross-validation was used on the training set using the Caret package, where the training set was split into ten subsets or folds (Figure S1b). One of the folds is left out for testing,

while the remainder is used to train the model. This process is repeated until all ten rows of folds are processed, generating a median R^2 (coefficient of determination) and RMSE value. All folds were again stratified to remove an imbalanced distribution of the models' target variable. The models were also examined using the testing sets, providing independent metric values. The model RMSE and R^2 values during cross-validation (CV) may differ slightly depending on how the training and testing sets are split. We thus repeated the workflow of random training/testing set splitting and 10-fold cross-validation ten times (Figure S1b). After model cross-validation and evaluation, the final saved models were trained on the full calibration dataset (i.e., Petrelli et al., 2020; Thomson et al., 2021).

3 P-T-H_2O-An models

3.1 Model calibration and validation

Figure 2 highlights the overall variation and median RMSE values from the cross-validation of both plagioclase-melt and melt hygrothermobarometry models. The plagioclase-melt and melt models for each variable (P-T-H_2O) depict a remarkably similar performance. The similarity across all models results from the predictive capability of the algorithm predominantly using the melt rather than the plagioclase compositional components (Figure 3), effectively rendering the plagioclase information redundant. This is unlike other random forest-calibrated models using mineral-melt pairs (clinopyroxene, Petrelli et al., 2020; biotite, Li and Zhang, 2022), where both the crystal and melt chemistry information improve the RMSE and R^2 scores. The melt model RMSEs also reaffirm the utility of silicate melt composition in recovering key magmatic variables (e.g. Helz and Thornber, 1987; Yang et al., 1996; Blundy, 2022; Weber and Blundy, 2024). This finding results from the low thermodynamic variance of natural magmatic compositions whose overall chemical variability can be described with a relatively limited number of independent compositional variables, significantly fewer than the total number of constituent oxides, as determined using Principal Component Analysis (Weber and Blundy, 2024). In this section, we will thus focus on the melt models, which are appropriate for use with compositions of quenched and entrapped

liquid (i.e. matrix glass or plagioclase-hosted melt inclusions). We will also examine limitations affecting model accuracy (i.e., model calibration) and precision (i.e., analytical uncertainties) to obtain P-T-H_2O estimates and compositions of plagioclase.

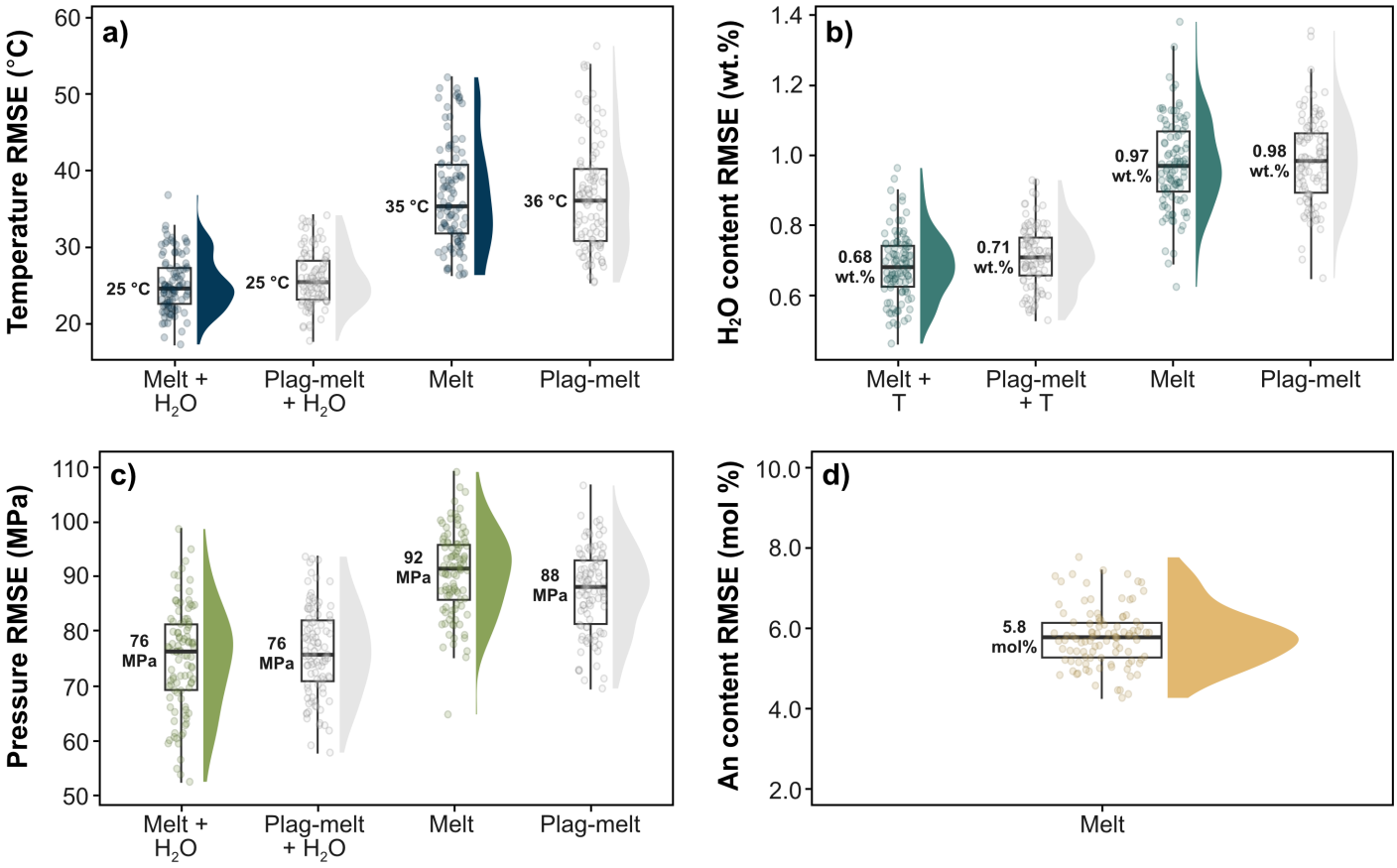

Figure 2. Raincloud comparison plots of cross-validation RMSEs from the plagioclase-melt and melt thermometer (**a**), hygrometer (**b**) and barometer (**c**) models, as well as the plagioclase anorthite content model (**d**).

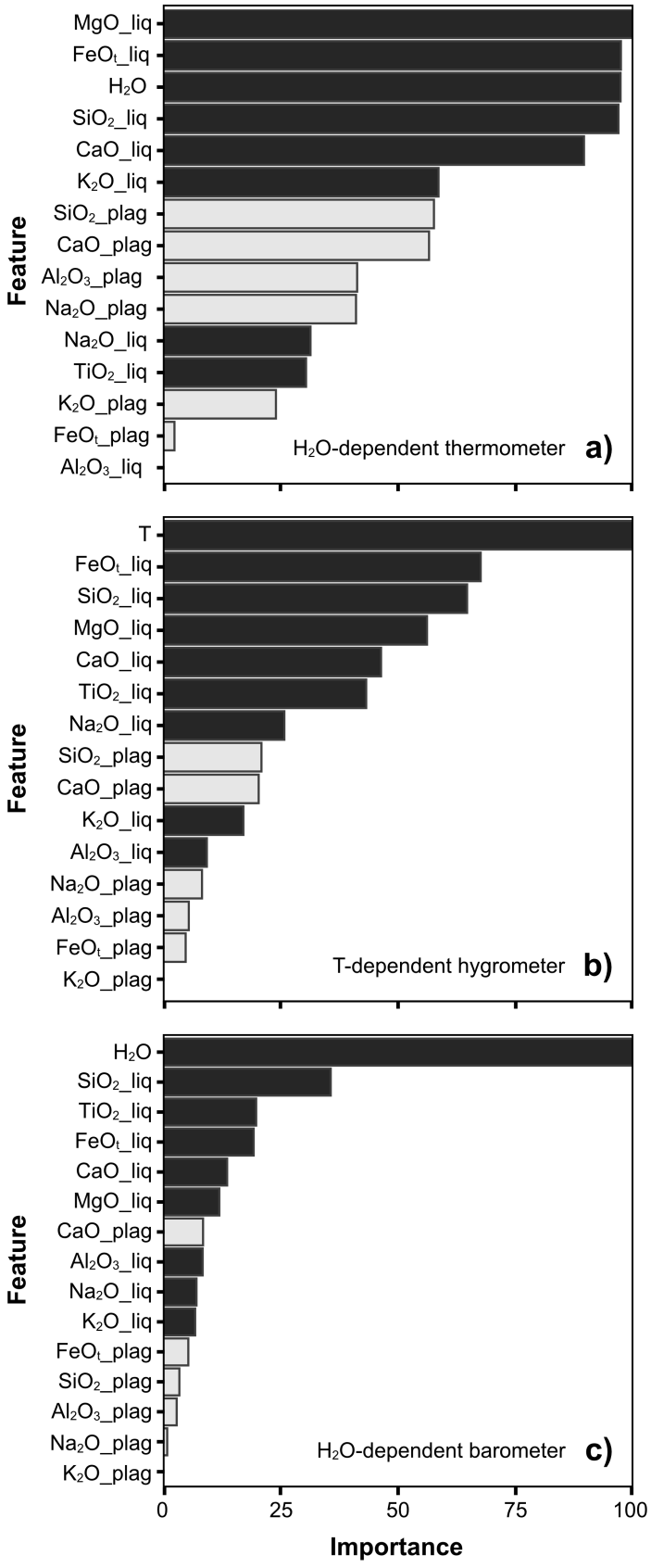
MgO_liq
FeOt_liq
H2O
SiO2_liq
CaO_liq
K2O_liq
SiO2_plag
CaO_plag
Al2O3_plag
Na2O_plag
Na2O_liq
TiO2_liq
K2O_plag
FeOt_plag
Al2O3_liq
Feature
H2O-dependent thermometer
a)
T
FeOt_liq
SiO2_liq
MgO_liq
CaO_liq
TiO2_liq
Na2O_liq
SiO2_plag
CaO_plag
K2O_liq
Al2O3_liq
Na2O_plag
Al2O3_plag
FeOt_plag
K2O_plag
Feature
T-dependent hygrometer
b)
H2O
SiO2_liq
TiO2_liq
FeOt_liq
CaO_liq
MgO_liq
CaO_plag
Al2O3_liq
Na2O_liq
K2O_liq
FeOt_plag
SiO2_plag
Al2O3_plag
Na2O_plag
K2O_plag
Feature
H2O-dependent barometer
c)
0
25
50
75
100
Importance

Figure 3. Plots of variable importance versus input variable for the H_2O-dependent thermometer (**a**), T-dependent hygrometer (**b**), and H_2O-dependent barometer (**c**). All plots highlight the most important variables used by the algorithm to make predictions. Light grey bars represent plagioclase compositional inputs, and dark grey bars represent melt oxide inputs along with additional parameters such as T or H_2O.

3.2 Thermometry

Temperature and H_2O in the experimental dataset display a strong inverse correlation (Figure 1d), leading us to test both an H_2O-independent and H_2O-dependent thermometer. In both instances, the H_2O-independent and H_2O-dependent thermometers yield low mean cross-validation (H_2O-independent, 35 °C; H_2O-dependent, 25 °C; Figure 2) and test set RMSE values (H_2O-independent, 38 °C; H_2O-dependent 26 °C). Systematic model errors were assessed by calculating the Mean Bias Error (MBE), as well as checking the regression gradients and intercepts (Wieser et al., 2023a). Both thermometers have relatively low intercept and MBE values with high gradients close to 1 (Figure 4b and Figure 5b), indicating no systematic offsets across the wide temperature range. Figures 4b and 5b display the test set residual distribution from all workflow replications and illustrate that 74% and 83% of residuals are within ± 30 °C of the actual experimental temperature for the H_2O-independent and H_2O-dependent thermometer, respectively. The accuracy of the thermometers primarily results from the strong non-linearity of MgO, SiO_2, FeO_t and CaO in the melt when plotted against temperature (Figure S2). This is consistent with other liquid thermometers that prioritise MgO, FeO_t and CaO within their parameterisations (e.g., Helz and Thornber, 1987). To further validate the ML models, we compare all our ML test set predictions (P-T-H_2O-An) with estimates generated by previous hygrothermobarometric and plagioclase-melt equilibria models (Figure 6). We use Thermobar (version 1.011; Wieser et al., 2023c) to calculate estimates from previous models but limit ourselves to models calibrated for a wide compositional range to ensure comparison across similar experimental conditions. We only compare our H_2O-dependent thermometer with the plagioclase-saturated liquid thermometer of Putirka (2008) (Equation 26; calibrated for T in the range 850–1350 °C), as both models require H_2O inputs. The ML H_2O-dependent thermometer performs better than Equation 26 with

a lower RMSE (26 °C vs. 36 °C), MBE (-0.94 °C vs. -9.6 °C) and intercept (41 °C vs. 112 °C) value, as well as a gradient and R^2 value closer to 1 (Figure 5b, Figure 6a).

3.2 Hygrometry

We tested a T-dependent (Figure 5c, 5d) and T-independent hygrometer (Figure 4c, 4d), as temperature is not always well-constrained in petrological studies. The T-dependent hygrometer (Figure 5c) returns median cross-validation and test set RMSE values of 0.68 wt.% and 0.69 wt.%, respectively, while the T-independent hygrometer (Figure 4c) gives reasonable cross-validation (0.97 wt.%) and test set (0.95 wt.%) RMSEs scores. No systematic offsets across the range of H_2O contents are apparent in the test data for both hygrometers, as they each have low intercept and MBE values and gradients close to 1 (Figure 4d, 5d). A closer look at the residuals, when grouped by type of experiment, reveals that the T-dependent hygrometer displays no difference in the modal and median values for anhydrous and hydrous ($X H_2O = 1$ and $X H_2O < 1$) experiments (Figure S3), with all groups concentrated at zero. For fluid-saturated experiments, the T-independent hygrometer residuals are centred at -1, indicating the model tends to slightly underestimate H_2O compared to fluid-undersaturated and anhydrous experiments. Temperature is an important variable in predicting melt water content, with 70% of the residuals for the T-dependent hygrometer within ±0.5 wt.% of the actual water content value (Figure 5d) compared to 58% of the residuals for the T-independent hygrometer (Figure 4d). Aside from temperature, FeOt, SiO_2 and MgO play a key role in water content predictions, in which the algorithm appears to use these three oxides to characterise H_2O content depending on the level of melt differentiation (Figure S4). These results broadly correspond with the findings of Zimmer et al. (2010), who show an inverse correlation exists between the level of Fe enrichment in melts (i.e., tholeiitic index) and their water content. We use the Putirka (2008; calibrated for liquids with <9 wt.% H_2O) and Waters and Lange (2015; calibrated for liquids with 0–8.3 wt.% H_2O) plagioclase-melt hygrometers to make a comparison with the T-dependent hygrometer, as all models require temperature inputs. The T-dependent hygrometer outperforms the Putirka (2008) and Waters and Lange (2015) plagioclase-melt

hygrometers with a lower overall RMSE (0.69 wt.%), MBE (-0.02 wt.%) and high gradient (0.94) and R^2 value (0.93; Figure 5d, Figure 6b).

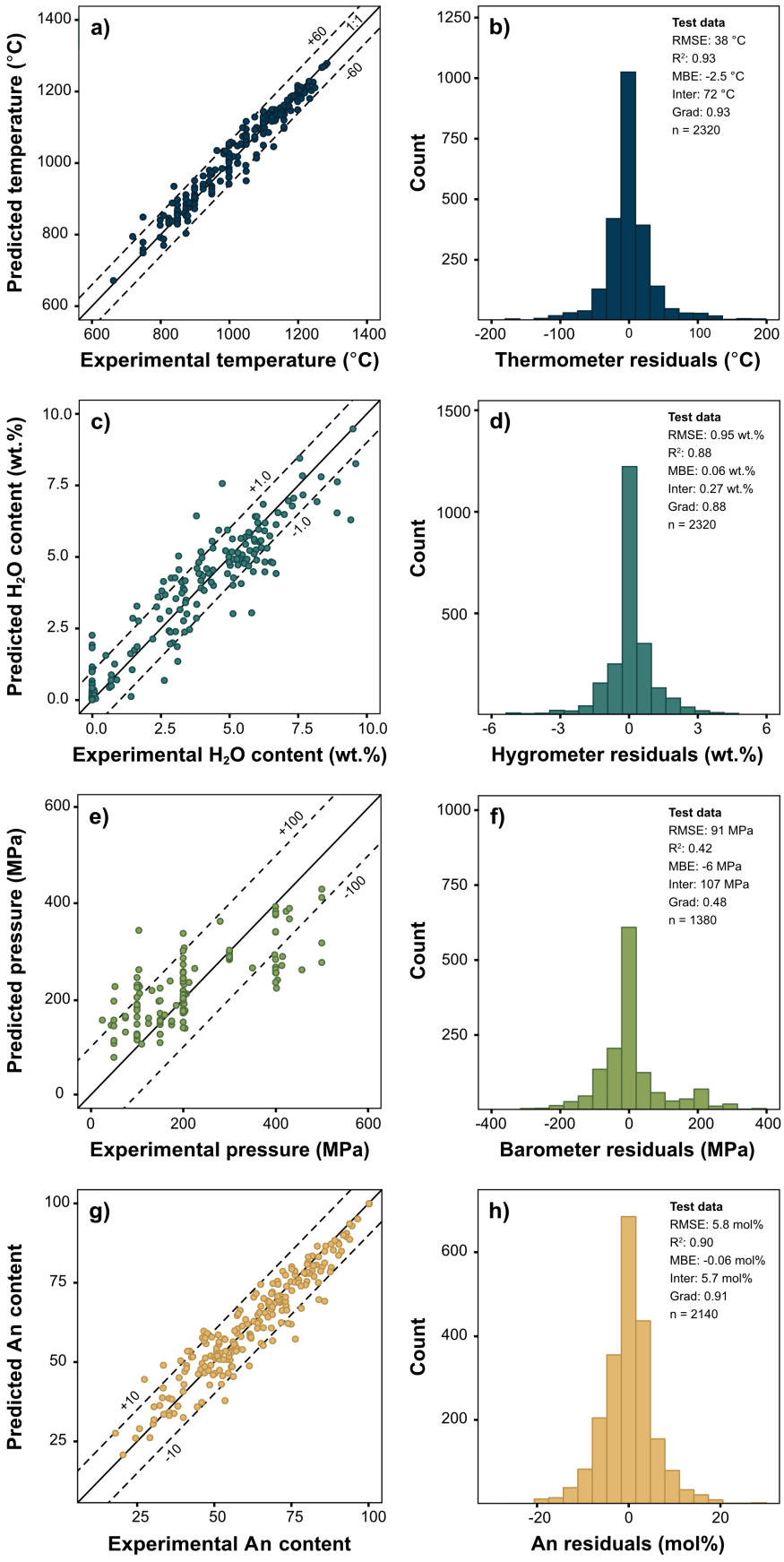
a)
Predicted temperature (°C)
Experimental temperature (°C)
+60
1:1
-60
b)
Test data
RMSE: 38 °C
R²: 0.93
MBE: -2.5 °C
Inter: 72 °C
Grad: 0.93
n = 2320
Count
Thermometer residuals (°C)
c)
Predicted H2O content (wt.%)
Experimental H2O content (wt.%)
+1.0
-1.0
d)
Test data
RMSE: 0.95 wt.%
R²: 0.88
MBE: 0.06 wt.%
Inter: 0.27 wt.%
Grad: 0.88
n = 2320
Count
Hygrometer residuals (wt.%)
e)
Predicted pressure (MPa)
Experimental pressure (MPa)
+100
-100
f)
Test data
RMSE: 91 MPa
R²: 0.42
MBE: -6 MPa
Inter: 107 MPa
Grad: 0.48
n = 1380
Count
Barometer residuals (MPa)
g)
Predicted An content
Experimental An content
+10
-10
h)
Test data
RMSE: 5.8 mol%
R²: 0.90
MBE: -0.06 mol%
Inter: 5.7 mol%
Grad: 0.91
n = 2140
Count
An residuals (mol%)

Figure 4. Examples of testing set performance for the melt-only models and residual (difference between experimental value and predicted value) histograms. Only the best-performing testing set is shown for each model. Testing set statistics in the histograms reflect the average RMSE, R^2, MBE, intercept and gradient values across all ten testing sets. **a**) Comparison of experimental versus predicted temperature (°C) showing a 1:1 correspondence line. **b**) Histogram for temperature residuals for all test sets. **c**) Comparison of experimental versus predicted water content (wt.%). **d**) Histogram of water content residuals for all test sets. **e**) Comparison of experimental versus predicted pressure (MPa). **f**) Histogram of pressure residuals for all test sets. **g**) Comparison of experimental versus predicted anorthite content (mol%). **h**) Histogram of anorthite content residuals for all test sets.

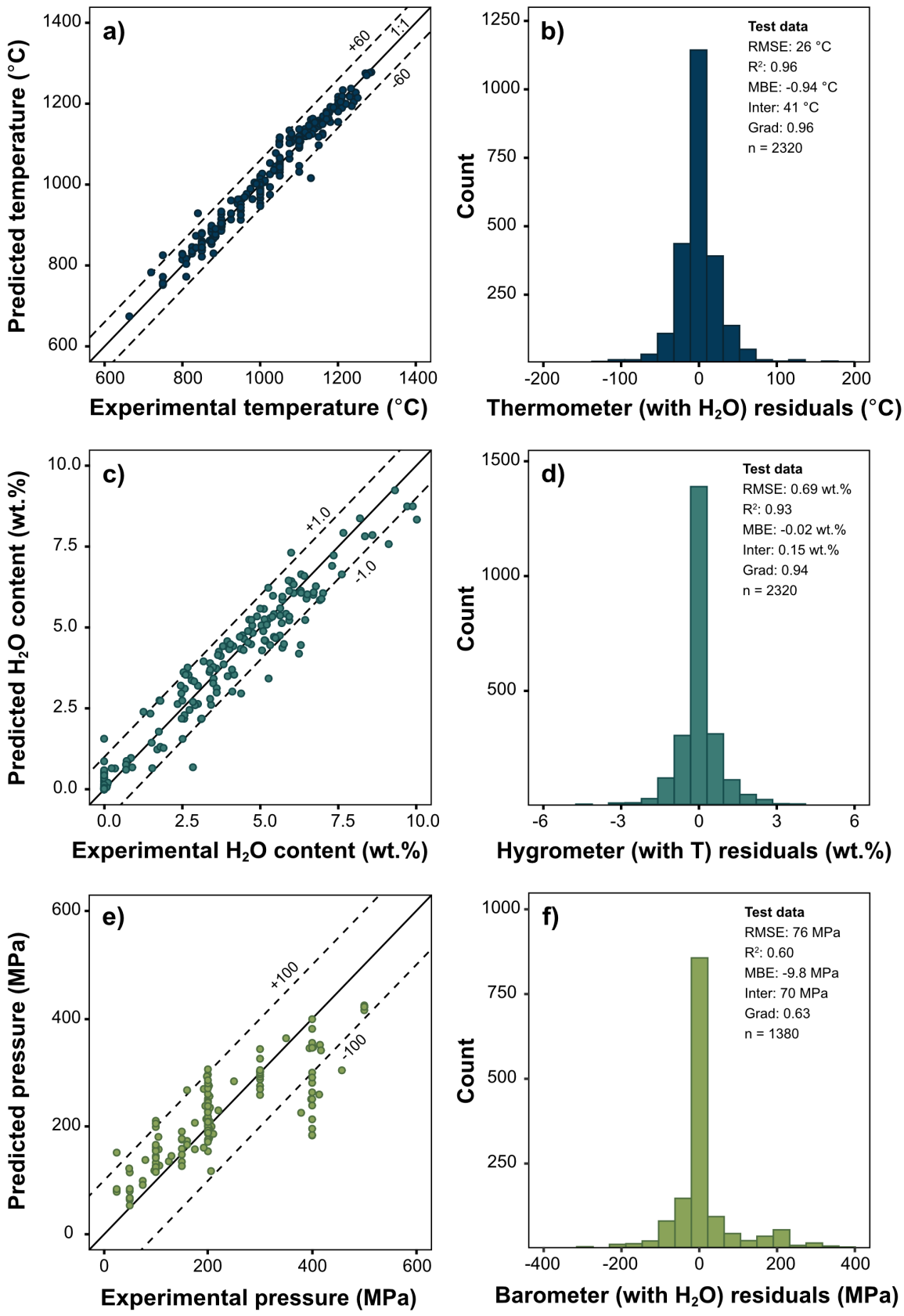
a)
+60
1:1
-60
Predicted temperature (°C)
Experimental temperature (°C)
b)
Test data
RMSE: 26 °C
R²: 0.96
MBE: -0.94 °C
Inter: 41 °C
Grad: 0.96
n = 2320
Count
Thermometer (with H2O) residuals (°C)
c)
+1.0
-1.0
Predicted H2O content (wt.%)
Experimental H2O content (wt.%)
d)
Test data
RMSE: 0.69 wt.%
R²: 0.93
MBE: -0.02 wt.%
Inter: 0.15 wt.%
Grad: 0.94
n = 2320
Count
Hygrometer (with T) residuals (wt.%)
e)
+100
-100
Predicted pressure (MPa)
Experimental pressure (MPa)
f)
Test data
RMSE: 76 MPa
R²: 0.60
MBE: -9.8 MPa
Inter: 70 MPa
Grad: 0.63
n = 1380
Count
Barometer (with H2O) residuals (MPa)

Figure 5. Examples of testing set performance for the melt models with additional input parameters (T or H_2O) and residual histograms. Only the best-performing testing set is shown for each model. Testing set statistics in the histograms reflect the average RMSE, R^2, MBE, intercept and gradient values across all ten testing sets. **a**) Comparison of experimental versus predicted temperature (°C) using a 1:1 correspondence line. **b**) Histogram for temperature residuals for all test sets. **c**) Comparison of experimental versus predicted water content (wt.%). **d**) Histogram of water content residuals for all test sets. **e**) Comparison of experimental versus predicted pressure (MPa). **f**) Histogram of pressure residuals for all test sets.

3.3 Barometry

We tested an H_2O-dependent (Figure 5e, 5f) and an H_2O-independent barometer (Figure 4e, f), as H_2O contents are not always well-constrained for natural systems, especially for lavas lacking glassy melt inclusions suitable for direct H_2O analysis. The barometers are calibrated using a reduced dataset by removing all high-pressure experiments (>500 MPa) due to the low number and narrow compositional range of experiments undertaken at higher pressures (Figure 1b). Atmospheric pressure experiments were also removed, as the pressure output for nominally anhydrous natural samples is likely to skew towards 0.1 MPa when H_2O is used as an additional input variable. Both barometers perform surprisingly well with 10-fold cross-validation (H_2O-dependent RMSE: 76 MPa; Figure 5e, f, H_2O-independent RMSE: 92 MPa, Figure 4e, f), which is confirmed by their predictive performance in the test set (H_2O-dependent RMSE: 76 MPa, H_2O-independent RMSE: 91 MPa; Figure 4e and 5e), although the R^2 values for both barometers are low (H_2O-dependent R^2: 0.60; H_2O-independent R^2: 0.42; Table S2). In terms of residuals, the addition of H_2O as an input enables 85% of the predictions to be within ±100 MPa of the actual experimental pressure for the H_2O-dependent barometer (Figure 5f), compared to 76% for the H_2O-independent (Figure 4f) barometer. None of the melt components has a dominant control on the pressure predictions, where it would be expected that Al_2O_3 and Na_2O would correlate with pressure (Blundy, 2022). Instead, the algorithm mainly uses SiO_2, TiO_2, FeO_t, MgO and CaO, suggesting that, like the hygrometers, the extent of differentiation helps constrain pressure values in a hypothetical P-T(-H_2O) space. The test set predictions for both barometers are systematically slightly offset as predictions <300 MPa tend to slightly overestimate pressures, while the barometers underestimate pressures >300 MPa, evident from the low gradient values and higher intercepts (Figure 4e and 5e). However, this pattern is similar to other barometers (e.g., clinopyroxene-based; Wieser et al., 2023b), likely amplified by the significant data gaps present at higher pressures in calibration datasets and the weak pressure trends with compositional variables. This highlights a crucial objective to conduct systematic experiments >300 MPa for a wide array of melt compositions to explore pressure correlations fully. To compare our H_2O-dependent barometer performance, we use the Putirka (2008) plagioclase-liquid

barometer (Equation 25a; calibrated for P <2000 MPa) due to both barometers requiring an H_2O input. A comparison of model performance statistics (Figure 5f, Figure 6c) for the ML and plagioclase-liquid barometer highlights that the ML barometer represents a significant improvement in reducing pressure estimate errors.

3.4 Anorthite content

We tested a model to estimate the composition of plagioclase (An content) as a function of the melt composition. The An model performs well without incorporating temperature and H_2O as additional input variables (Figure 4g, 4h), with a median 5.8 mol% RMSE during cross-validation (Figure 2d) and a 5.8 mol% RMSE for the test set data (Figure 4g). The test data show no overall systematic offset across the An content range with low intercept and MBE values and a gradient close to 1 (Figure 4g), attesting to the model's high accuracy of anorthite predictions. Furthermore, 69% of the predictions have residuals within ± 5 mol% of the measured values and 91% within ± 10 mol%. CaO, SiO_2 and MgO in the melt are the dominant controls on plagioclase anorthite content (Figure S5), consistent with thermodynamic and experimental studies (e.g., Panjasawatong et al., 1995; Namur et al., 2012; Neave and Namur, 2022). With temperature exerting a primary control on plagioclase composition (e.g., Kudo and Weill, 1970; Lange et al., 2009; Figure 1c), the combination of CaO, SiO_2 and MgO also likely acts as an indirect proxy for temperature aiding anorthite predictions. We test our ML anorthite model against model E of Putirka (2005), calibrated on experiments with SiO_2 contents of 42–73 wt.% and plagioclase compositions of An_{40-95} (Figure 6d). We also compare the anhydrous test set experiments with the T-independent models (Eq. 33–35) of Namur et al. (2012) that are all calibrated on 0.1 MPa experiments with SiO_2 contents of 43–78 wt.% and plagioclase compositions of An_{39-100}. The ability of the ML model to predict equilibrium plagioclase compositions is greater than that of model E (Figure 6d; e.g., RMSE: 14 mol%), whereas, for the subset of anhydrous experiments, Namur et al.'s (2012) T-independent empirical models (Eq. 33–35) have comparable

RMSE, intercept and gradient values to the ML model, although the latter has a lower MBE and a higher R^2 value (Figure 4h, Figure 6d).

3.5 Plagioclase saturation

Before using any of the models, melt compositions must first be checked for plagioclase saturation to avoid erroneous model predictions, which may prove difficult if petrographic or microanalytical analyses cannot be carried out on samples, for example, in cases where only bulk rock data are available. We have thus developed a classifier model to screen matrix glass compositions for plagioclase saturation. We compiled an approximately equal amount of non-plagioclase to plagioclase-saturated experimental data (n_{total} = 2206) for calibration (Table S3) and used the classification mode of the algorithm to train the model. The classifier cross-validation process is the same as all the regression models outlined in Section 2.2, but 5-fold cross-validation was used instead. We use the classification accuracy metric to evaluate the classifier's performance, which is a ratio describing the number of correct predictions to the total number of predictions. The mean accuracy from cross-validation and test sets is 87% and 90%, respectively. Table S4 presents an average test set confusion matrix, which summarises all sets of classification results (i.e., false positive, false negative, true positive, true negative) from all test set replications and indicates low rates of false positive (~4%) and false negative (~5%) classifications. SiO_2, MgO and Al_2O_3 are the main melt oxides used to classify plagioclase saturation, corresponding to SiO_2 and MgO acting as differentiation and temperature proxies and Al_2O_3 indicating the onset of plagioclase crystallisation.

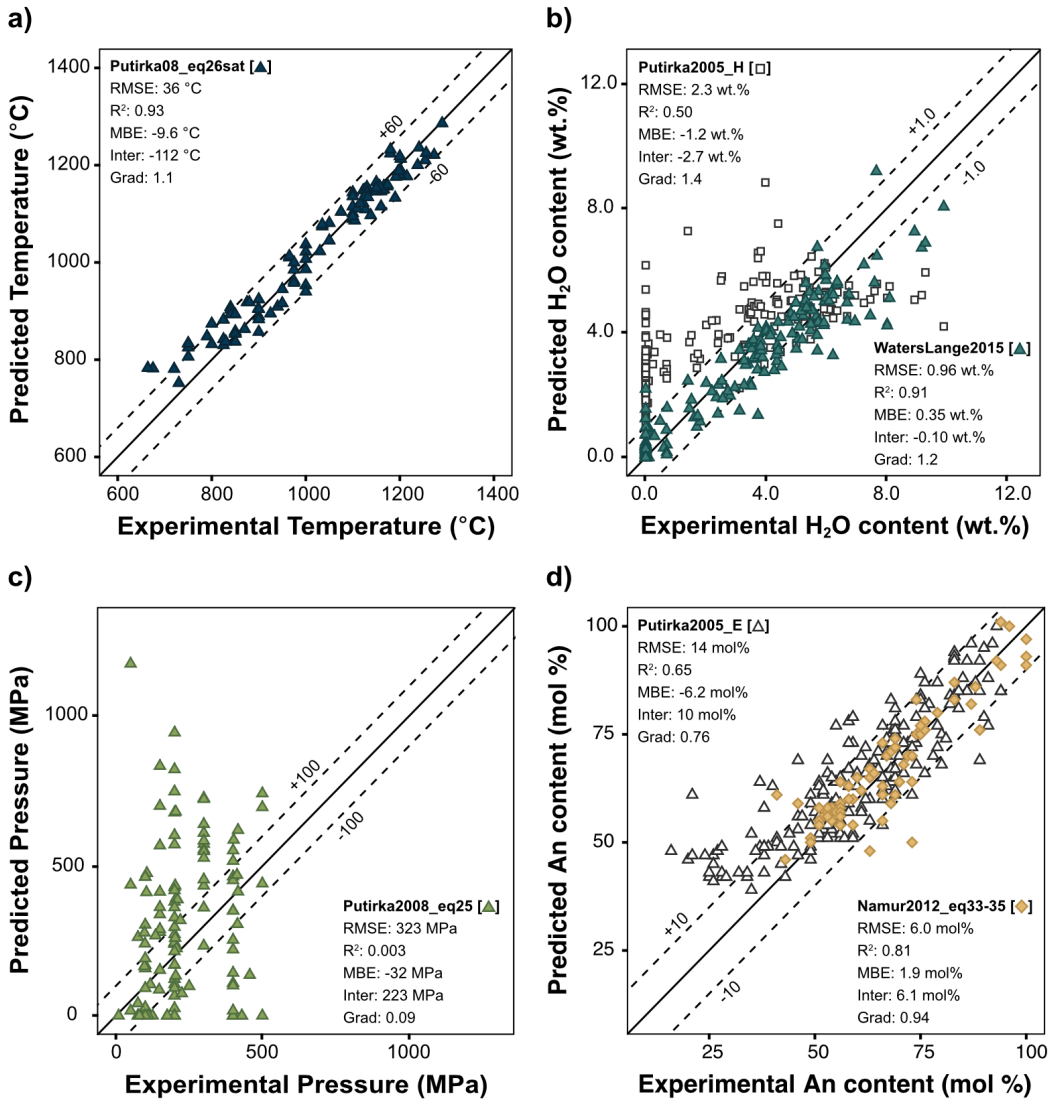

Figure 6. Testing set performance using other plagioclase-melt or melt models. Only the best-performing testing set is shown for each model, but the testing set statistics reflect the average RMSE, R^2, MBE, intercept and gradient values across all ten testing sets. **a**) Plot of experimental temperature versus the predicted temperature (°C) derived from liquid thermometer (Equation 26) of Putirka (2008). **b**) Plot of experimental water contents versus the predicted water contents (wt.%) resulting from plagioclase-melt hygrometers of Putirka (Model H; 2008) and Waters and Lange (2015). **c**) Plot of experimental pressure versus the predicted pressure (MPa) resulting from the plagioclase-melt barometer (Equation 25) of Putirka (2008). **d**) Plot of experimental anorthite content versus the predicted anorthite content (mol%) derived from the plagioclase-melt equilibria model of Putirka (Model E; 2008) and Namur et al. (Equations 33–35; 2012).

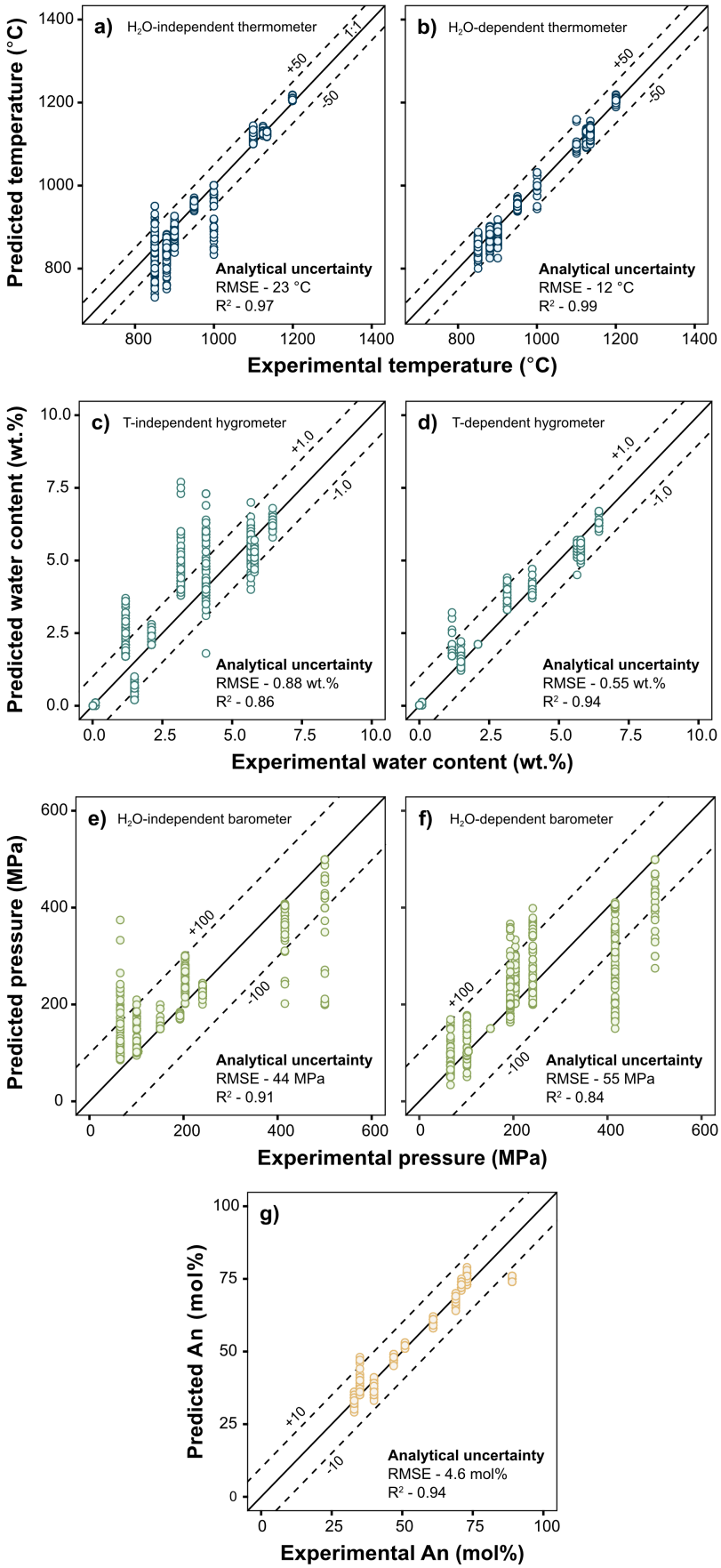
a) H2O-independent thermometer
1:1
+50
-50
Analytical uncertainty
RMSE - 23 °C
R² - 0.97
b) H2O-dependent thermometer
+50
-50
Analytical uncertainty
RMSE - 12 °C
R² - 0.99
Predicted temperature (°C)
Experimental temperature (°C)
c) T-independent hygrometer
+1.0
-1.0
Analytical uncertainty
RMSE - 0.88 wt.%
R² - 0.86
d) T-dependent hygrometer
+1.0
-1.0
Analytical uncertainty
RMSE - 0.55 wt.%
R² - 0.94
Predicted water content (wt.%)
Experimental water content (wt.%)
e) H2O-independent barometer
+100
-100
Analytical uncertainty
RMSE - 44 MPa
R² - 0.91
f) H2O-dependent barometer
+100
-100
Analytical uncertainty
RMSE - 55 MPa
R² - 0.84
Predicted pressure (MPa)
Experimental pressure (MPa)
g)
+10
-10
Analytical uncertainty
RMSE - 4.6 mol%
R² - 0.94
Predicted An (mol%)
Experimental An (mol%)

Figure 7. Monte Carlo simulations of electron microprobe analytical errors and their effect on resulting temperatures (**a**, H_2O-independent thermometer; **b**, H_2O-dependent thermometer), water contents (**c**, T-independent hygrometer; **d**, T-dependent hygrometer), pressures (**e**, H_2O-independent barometer; **f**, H_2O-dependent barometer), and anorthite content estimates (**g**).

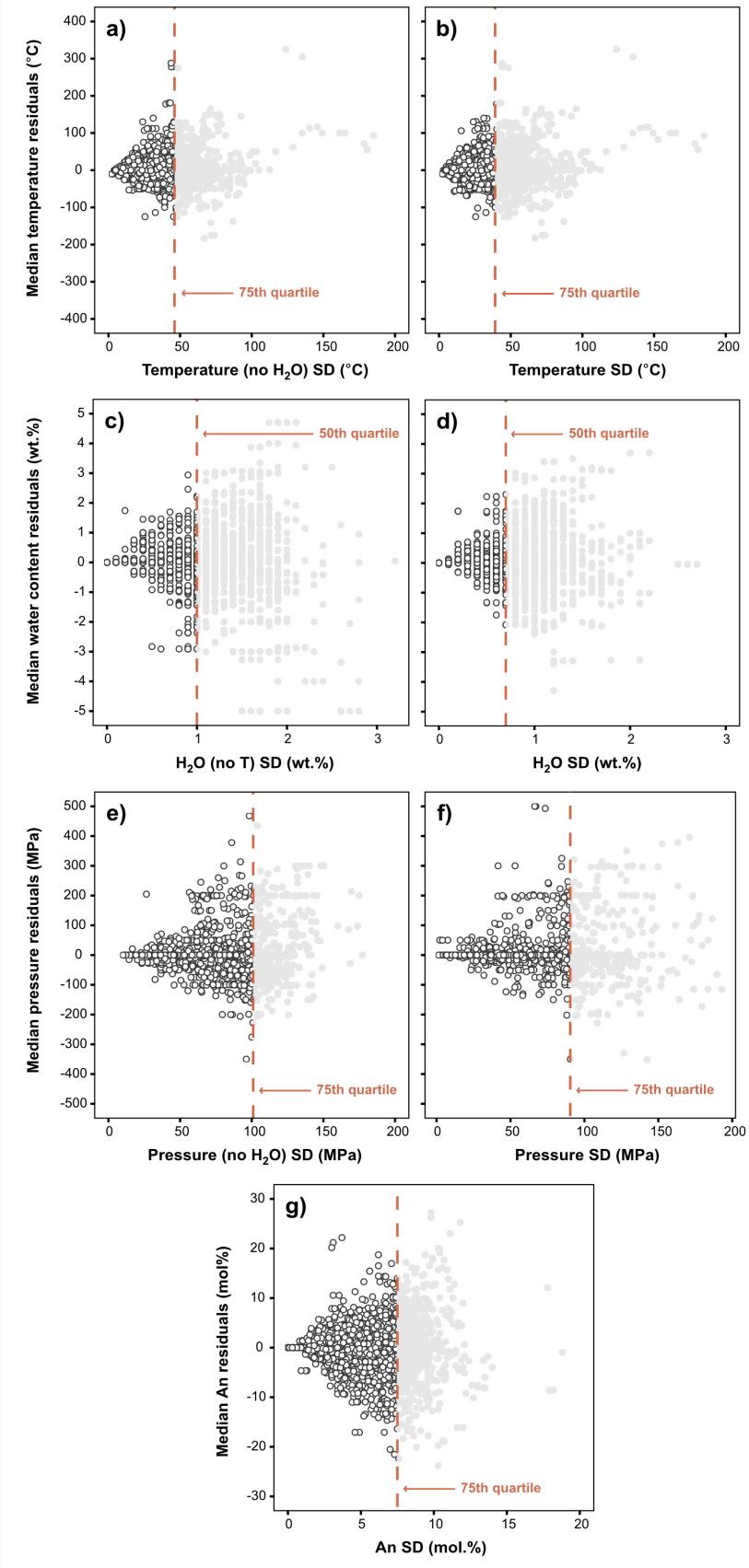
a)
b)
c)
d)
e)
f)
g)
Median temperature residuals (°C)
Median water content residuals (wt.%)
Median pressure residuals (MPa)
Median An residuals (mol%)
75th quartile
50th quartile
Temperature (no H2O) SD (°C)
Temperature SD (°C)
H2O (no T) SD (wt.%)
H2O SD (wt.%)
Pressure (no H2O) SD (MPa)
Pressure SD (MPa)
An SD (mol.%)

Figure 8. Investigation of appropriate filters for all testing set P-T-H_2O-An estimates using the standard deviation. Dashed lines highlight the 50^{th} or 75^{th} standard deviation quartile, where estimates (light grey points) greater than this value should be removed. The testing set statistics reflect the average RMSE, R^2, MBE, intercept and gradient values across all ten testing sets after filtering. **a**) Median temperature residuals versus temperature SD (°C) for the H_2O-independent thermometer. **b**) Median temperature residuals versus temperature SD (°C) for the H_2O-dependent thermometer. **c**) Median water content residuals versus water content SD (wt.%) for the T-independent hygrometer. **d**) Median water content residuals versus water content SD (wt.%) for the T-dependent hygrometer. **e**) Median pressure residuals versus pressure SD (MPa) for the H_2O-independent barometer. **f**) Median pressure residuals versus pressure SD (MPa) for the H_2O-dependent barometer. **g**) Median anorthite content residuals versus anorthite content SD (mol%) for the plagioclase-melt equilibria model.

3.6 Further model limitations

The P-T-H_2O bounds of the calibration dataset represent one major limitation of all models. The models presented here should *never* be used outside the calibration range since the ML algorithm is unsuited for extrapolation. Additional experimental constraints covering key calibration dataset gaps will help to increase model accuracy (i.e., Figure 1). Furthermore, hygrometer RMSEs could be improved if more experimental glasses were analysed for H_2O to increase the number of direct H_2O measurements within the calibration dataset, rather than using indirect H_2O estimates from solubility models (e.g., Papale et al., 2006; Zhang et al., 2007; Ghiorso and Gualda, 2015) or the 'volatiles by difference' method (e.g., Devine et al., 1995) that can have large uncertainties (e.g., Hughes et al., 2019). This is particularly true for low-H_2O melts.

The precision of P-T-H_2O-An predictions is influenced by the analytical error of the melt composition itself (e.g., Gualda and Ghiorso, 2014; Wieser et al., 2023d). To evaluate the impact of analytical (i.e. electron microprobe; EPMA) uncertainties on P-T-H_2O-An predictions, we used a series of Monte Carlo simulations to create major element oxide variation based on ten melt compositions (Table S5). These ten melts were chosen to represent the compositional range and experimental conditions throughout the calibration dataset. For each melt, new compositions are generated from its original oxide values with noise added from a normal distribution, with the variation deriving from a weighted mean of one sigma standard deviation EPMA values (Table S5) from a subset of experiments (n=400). The ten melts generated 2000 melt compositions by running a 200-time simulation per composition and subsequently used as inputs for each melt model. The simulations for the melt-only models highlight that analytical errors impose a limit on precision of ±44 MPa for pressure, ±23 °C for temperature, ±0.56 wt.% for H_2O (with temperature), ±0.88 wt.% for H_2O (without temperature) and ±4.6 mol % for anorthite content (Figure 7a-g). In addition, analytical uncertainties associated with H_2O content inputs measured by SIMS or FTIR/Raman spectroscopy were also tested using a pessimistic averaged standard deviation of 0.5 wt.% (Ulmer et al., 2018), as few studies provide sufficient information (e.g., the number

of analyses, standard deviations of water measurements) to calculate a reliable weighted mean. The simulations indicate that melt and water analytical errors can limit H_2O-dependent model precision to ±55 MPa for pressure and ±12 °C for temperature (Figure 7b, 7f). Both sets of simulations indicate the sensitivity of our hygrothermobarometers to analytical uncertainty. The simulations emphasise the need to undertake careful preparation (i.e., tephra extraction, Cooper et al., 2019; glass alteration recognition) and analytical procedures (i.e. EPMA; Hayward, 2012) of matrix glass and inclusions to minimise the chemical variability of susceptible oxides (e.g., MgO, SiO_2) that would affect subsequent predictions.

4 Model application

To test the calibrations of our melt models, we have applied them to two tectonically contrasting, well-constrained volcanic systems (Mount St Helens, USA; Bárðarbunga, Iceland). We compare the predicted values to previous estimates calculated from various thermobarometers, direct H_2O measurements from melt inclusions and seismic information about the sub-volcanic systems. For each application, we also discuss the different ways the models can be used depending on whether the melt H_2O contents are known, along with suggestions on P-T-H_2O-An and plagioclase saturation prediction filtering.

4.1 May–October 1980 eruption, Mount St Helens, USA

On May 18th 1980, the north flank of Mount St Helens' edifice collapsed, depressurising the shallow magmatic ‘cryptodome’ and triggering a lateral blast. Eruption of a 24 km-high Plinian column ensued later that day as depressurisation reached the deeper magmatic system. Smaller explosive eruptions characterise subsequent activity from May to October 1980; a series of dome-forming extrusions within the crater followed through to October 1986. Here, we apply the models to matrix glass and plagioclase-hosted melt inclusion data (*n*=151) in Blundy et al. (2008) from the 1980 eruptive activity of Mount St Helens. The erupted magma was a porphyritic dacite (or silicic andesite) with ~63 wt.% SiO_2 and ~35 vol% phenocrysts. The melt phase, both as inclusions and matrix glass, was uniformly rhyolitic and thought to be

saturated in plagioclase, orthopyroxene, magnetite and ilmenite (Rutherford et al., 1985). Amphibole also occurs as a phenocryst phase but shows some evidence of resorption or breakdown, notably in the dome-forming magmas. Clinopyroxene is a rare phenocryst phase in some samples.

In cases where constraints for all variables (P-T-H_2O-An) are unknown, the variables should be recovered sequentially in the following order: An → T → H_2O → P (Figure S6). Before using the P-T-H_2O models, glass compositions must demonstrate that they represent a melt in equilibrium with plagioclase, which can be achieved by comparing An predictions from the plagioclase-equilibria model with natural plagioclase rim compositions. The uncertainty of a prediction is given as the standard deviation and can be used to filter model predictions to further reduce errors. This has been shown by Weber and Blundy (2024), where their model test set predictions using a random forest algorithm display higher residual variance as the standard deviation (SD) increases. Figure 8 presents our melt model test set residuals against the SD and shows most of the divergence begins from the 75th quartile of SD values. In addition, our test set statistics display an improvement with overall lower RMSE, intercept, and MBE values with higher gradients and R^2 values, especially in the case of the barometers (Figure 8e, f). Therefore, we recommend filtering values by removing the top 25% SD values. However, for the hygrometers, removing values above the 50th quartile is more effective at reducing the variance (Figure 8). Although filtering will lead to fewer predictions, removing predictions with the highest variance will ensure more robust estimates. Accordingly, we only report the filtered estimates from all models with both applications (Table S6).

The range of plagioclase compositions in equilibrium with the compositional range of plagioclase-hosted melt inclusions and matrix glasses is estimated at An_{21-51} (matrix mode: 45 mol%; MI mode: 39 mol%), which corresponds within error to the

dominant plagioclase rim composition (An_{47}; Berlo et al., 2007), suggesting that the plagioclase rims were in equilibrium with the host melt.

The H_2O-independent thermometer returns mean melt inclusion and matrix glass temperatures of 892 ± 55°C (SD) and 885 ± 49°C (Fig. 9a), respectively; the former is consistent with melt inclusion temperatures (853–941 °C; Blundy et al. 2006) calculated using the plagioclase-liquid thermometer of Putirka (2005). Fe-Ti oxide thermometry estimates (816–958 °C; Blundy et al., 2008), calculated using the oxide recalculation procedure of Spencer and Lindsley (1981) and the thermometer of Andersen and Lindsley (1988), extend the range to slightly higher temperatures. This slight magma heating may reflect latent heat release due to crystallisation or magma recharge (Blundy et al., 2006) and the ability of Fe-Ti oxides to re-equilibrate chemically on short timescales (Venezky & Rutherford, 1999).

We next use the predicted melt temperatures as inputs for the T-dependent hygrometer, producing H_2O estimates between 2.6 and 6.5 wt.%. We also performed Monte Carlo error propagation using the temperature SD from the thermometer outputs (Figure 9a), and the mean uncertainty for H_2O predictions across all samples is ± 1.4 wt.%. A full description of the error propagation method is presented in Text S1. The majority of melt inclusion H_2O estimates are broadly similar to measured analyses by SIMS (Blundy et al., 2006). In contrast, the estimated H_2O contents for the groundmass and the highly silicic (>75 wt.% SiO_2) melt inclusions are significantly higher than measured (Figure 9b) values, reflecting extensive degassing upon eruption and the failure of the melt to evolve chemically in response (Blundy and Cashman, 2005). The comparison could also signify a deficit of highly silicic calibration experiments with low dissolved water concentrations where the H_2O estimates diverge more profoundly from the 1:1 line. Furthermore, Figure 9b highlights that H_2O content negatively correlates with SiO_2, consistent with Blundy and Cashman (2005) suggesting decompression crystallisation of the groundmass and plagioclase phenocrysts during ascent.

Finally, using the predicted H_2O contents as inputs for the H_2O-dependent barometer, the pressure predictions returned values between 50 and 250 MPa (matrix

mean: 117 ± 44 MPa, melt inclusion mean: 98 ± 41 MPa; Figure 9a). We again performed error propagation using the water uncertainty from the hygrometer resulting in a mean uncertainty of ± 38 MPa across all samples. The mean uncertainties for both H_2O and pressure highlight that even with two unknown variables for a system, the accumulated errors are still low enough to obtain informative interpretations; we include the error propagation capability within the provided R scripts (Cutler, 2024). The H_2O-independent barometer returns similar pressures of 44–225 MPa (matrix mean: 113 ± 59 MPa, melt inclusion mean: 109 ± 61 MPa; Figure 9a). The pressures, particularly from melt inclusions, overlap with saturation pressure values (melt inclusion range: 7–282 MPa; mean: 97 MPa, matrix range: 3.2–20.6 MPa; matrix mean: 8.3 MPa; Figure 9a) from Blundy et al. (2010) estimated using Papale's et al. (2006) H_2O-CO_2 solubility model. Overall, the main pressure range (44–250 MPa) resulting from both barometers convert to depths of 1.2–6.9 km using a 2700 kg/m^3 average crustal density. Scandone and Malone (1985) estimated a reservoir depth of 7–9 km using net edifice subsidence measured from electronic tiltmeters. An aseismic zone was also mapped at 7 km extending vertically for 6+ km from earthquake hypocentres, and interpreted as a reservoir connected to the surface (Scandone and Malone, 1985; Lees, 1992). Although our mean melt inclusion and matrix glass crystallisation depths are shallower than geophysical estimates, the glass compositions likely record crystallisation conditions during pre-eruptive ascent from the top of the storage region, consistent with the H_2O vs. SiO_2 relationship in Figure 9b.

4.2 2014-2015 Holuhraun eruption, Bárðarbunga, Iceland

In mid-August 2014, a dyke propagated laterally NE from Bárðarbunga volcano, and by the end of August, the dyke caused a fissure eruption at the Holuhraun lava field (Ágústsdóttir et al., 2016). The Holuhraun magma was a phenocryst poor (≤5 vol%), highly vesicular olivine tholeiite (Halldórsson et al. (2018). Here, we use the basaltic matrix glass and plagioclase-hosted melt inclusion (with post-entrapment crystallisation corrections) data (*n*=251) from Hartley et al. (2018) and Halldórsson et al. (2018). Matrix glass data points with <6 wt.% MgO were removed, as they represent syn-emplacement crystallisation conditions (Halldórsson et al., 2018). We tested the plagioclase-saturation

classifier on the matrix glasses (*n*=175), and 174 compositions are predicted to be plagioclase-saturated, in agreement with the petrography of the samples (plagioclase-olivine-clinopyroxene-Fe-Ti oxides; Halldórsson et al., 2018). Although the one matrix glass composition that failed the classifier test could be, in fact, plagioclase-saturated (i.e., false negative), the main objective of the classifier approach is to eliminate any false positives that may generate inaccurate pressure estimates. We thus removed that single matrix glass composition for subsequent P-T-H_2O-An estimations.

The modal equilibrium plagioclase compositions predicted for matrix glasses and melt inclusions are An_{70} and An_{79}, respectively, consistent with the estimated equilibrium plagioclase phenocryst rims and microphenocrysts using the plagioclase-melt equilibria model of Namur et al. (2012) ($An_{64.5–75}$; Halldórsson et al., 2018; Figure 10a). A subset of melt inclusions with higher MgO contents (>8 wt.%) have higher An_{75-82} contents, which likely represent the entrainment of plagioclase phenocrysts from mush horizons (Hartley et al., 2018) now in disequilibrium with the surrounding melt.

Temperature reconstructions for matrix glasses and melt inclusions (<8 wt.% MgO) with the H_2O-independent thermometer yield mean temperatures of 1157 ± 14 °C and 1176 ± 13.5 °C (Figure 10b), respectively, consistent with clinopyroxene-liquid thermometry (1161 ± 11 °C; Neave et al., 2019) using Eq. 33 of Putirka (2008), whereas the primitive melt inclusions (higher MgO) record a higher mean temperature of 1203 ± 13 °C (Figure 10b). Water contents in matrix glasses and melt inclusions have been measured by FTIR and calculated, accounting for diffusive re-equilibration of melt inclusions, to be in the range of 0.13–0.7 wt.% (Bali et al., 2018; Hartley et al., 2018). If water contents are constrained to a specific range, we can use the H_2O-dependent barometer differently by testing various water values as inputs. We use values of 0.0, 0.3, 0.6 and 0.9 wt.% (Figure 10b), and the barometer returns matrix glass pressures of 151–296 MPa (mean: 185 ± 94 MPa) and melt inclusion pressures of 116–300 MPa (mean: 164 ± 99 MPa) for all water contents; varying the water content results in only minor pressure differences (~10–25 MPa). The H_2O-independent barometer gives similar matrix glass and melt inclusion pressures ranging between 191–202 MPa (mean: 191 ± 97 MPa) and 176–300 MPa (mean: 176 ± 91 MPa), respectively. All mean

pressure predictions are in good agreement (Figure 10c) with pressures estimated by clinopyroxene-liquid barometry (232 ± 86 MPa, Neave et al., 2019; using iterative thermobarometric calculations including Eq. 1 of Neave and Putirka, 2017 and Eq. 33 of Putirka, 2008), plagioclase-liquid barometry (141 ± 247 MPa, Geiger et al., 2014; using Eq. 25a of Putirka, 2008), and OPAM thermal minima (matrix glass: 210 ± 70 MPa, melt inclusion: 350 ± 170 MPa) with OPAM pressures for primitive melt inclusions returning values of 300–350 MPa (Hartley et al., 2018). Using a crustal density of 2860 kg/m^{-3} (Carlson and Herrick, 1990), the ML barometer pressures convert to depths of 3.4–8.8 km. These depths correspond well with the location of earthquake hypocentres (5–7 km; Figure 10c) associated with dyke propagation prior to the eruption (Sigmundsson et al., 2015; Ágústsdóttir et al., 2019).

Overall, the plagioclase-saturated melt models are effective at identifying the last-equilibrated composition of plagioclase crystals with the host melt and characterising key intensive variables at both Mount St Helens and Bárðarbunga. This is shown by the generally good agreement of predictions with previous petrological estimates using different models (e.g., volatile solubility and mineral $\pm$ melt thermobarometry) and geophysical data. Comparison of direct H_2O measurements with hygrometer predictions may also provide insight into which melt inclusions have likely lost water during ascent and their original water contents. The models offer the additional benefit of not requiring saturation of a specific mineral assemblage, which can often restrict the application of many melt-based models (e.g., olivine-plagioclase-augite, OPAM, Yang et al., 1996; Rhyolite-MELTS; Gualda and Ghiorso, 2014).

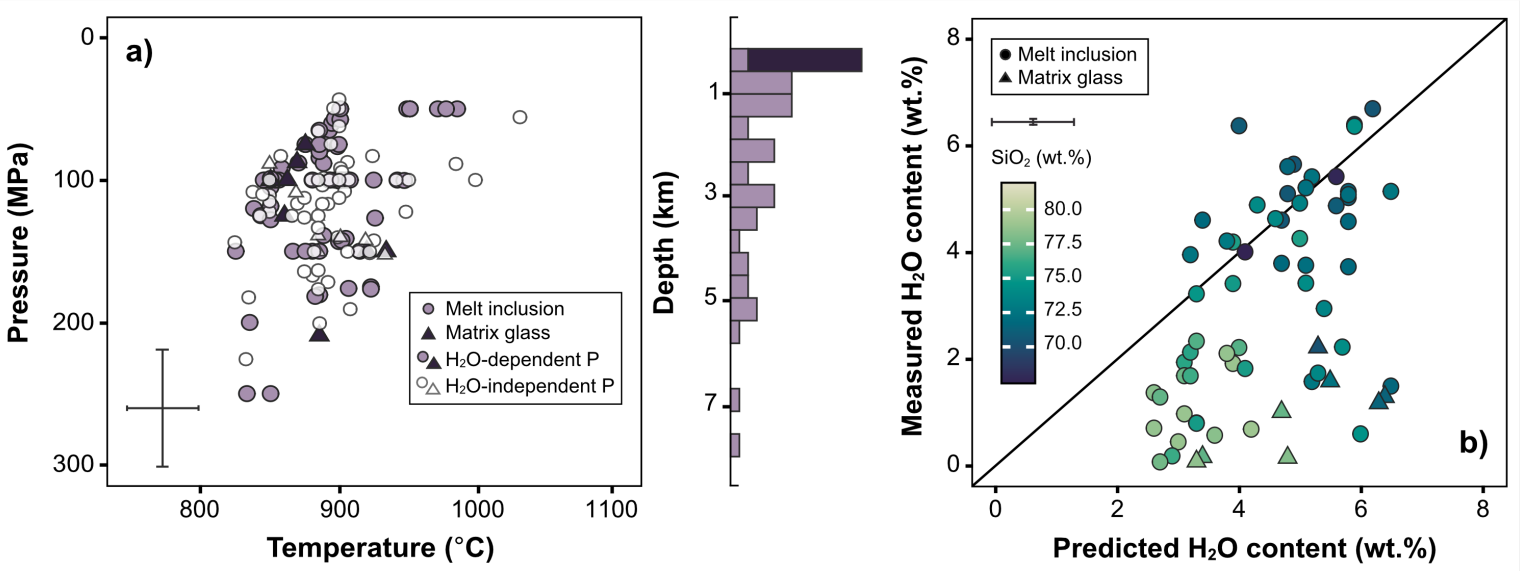

Figure 9. a) Filtered temperature (°C) vs. pressure (MPa) predictions of melt inclusions and matrix glasses (*n*=113) for the 1980 Mount St Helens eruption, estimated using the H_2O-independent melt thermometer, H_2O-dependent melt barometer, and H_2O-independent melt barometer. The histogram on the right displays the saturation pressures of matrix glass (*n*=29) and melt inclusions (*n*=45) from Blundy et al. (2010), estimated using the Papale et al. (2006) solubility model. **b**) SIMS water contents versus predicted water contents using the T-dependent hygrometer. Colour coding reflects SiO_2 content (wt.%) in melt.

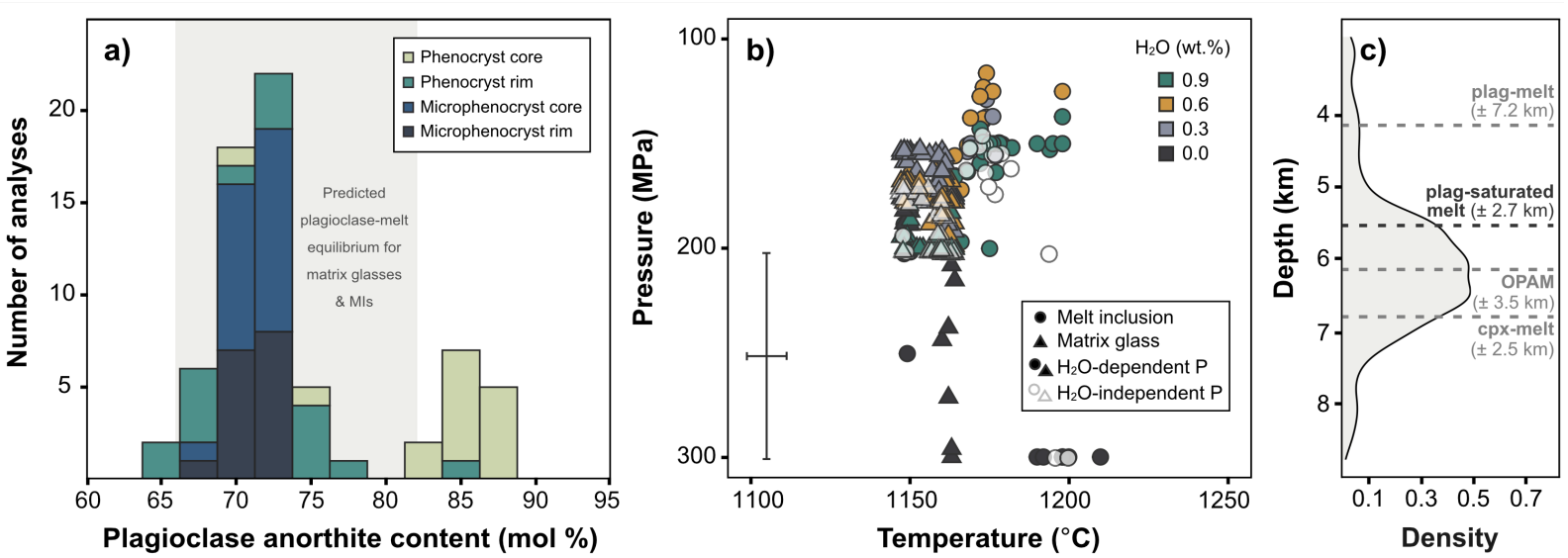

Figure 10. a) Stacked histogram displaying the composition of plagioclase phenocrysts and microphenocryst crystals from the 2014-2015 Holuhraun eruption (data from Halldórsson et al. (2018), with the light grey field representing the plagioclase compositions predicted to be in equilibrium with the carrier liquid and inclusions. **b**) Filtered temperature (°C) versus pressure (MPa) predictions of melt inclusions and matrix glasses (*n*=248) for the 2014-2015 Holuhraun eruption, calculated using the H_2O-independent melt thermometer, H_2O-dependent melt barometer, and H_2O-independent melt barometer. Colour coding depicts the H_2O content (wt.%) used as H_2O-dependent barometer input. **c**) Density distribution of dyke seismicity (15th to 30th August 2014; *n*=273) prior to the eruption; data taken from Ágústsdóttir et al. (2019). Dashed lines represent mean depths estimated from plagioclase-liquid barometry (Geiger et al., 2014) using Eq. 25a (Putirka, 2008), plagioclase-saturated melt barometry (mean of both matrix glass and melt inclusion pressures estimated from both H_2O-dependent and H_2O-independent melt barometers), OPAM barometry (Hartley et al., 2018), and clinopyroxene-liquid barometry (Neave et al., 2019) using iterative thermobarometric calculations of Eq. 1 of Neave and Putirka (2017) and Eq. 33 of Putirka (2008).

5 Conclusions

We have tested various plagioclase-based hygrothermobarometric models using either plagioclase-melt or melt chemistry and developed an updated plagioclase-melt equilibria model, with all models calibrated using random forest machine learning. Our results show that the melt compositional information holds nearly all the P-T-H_2O information rather than the plagioclase, resulting in the melt and plagioclase-melt models returning incredibly similar cross-validation RMSE values. Test set RMSEs for the melt + T/H_2O and melt-only models are 25°C–35°C, 0.65 –1.00 wt.%, 74–88 MPa and 5.8 mol% for temperature, water content, pressure and anorthite content, respectively. In general, the models provide an enhanced prediction accuracy for P-T-H_2O and anorthite content values. Furthermore, the T and H_2O-independent melt hygrothermobarometers allow predictions to be obtained without requiring additional inputs (P/T/H_2O) that are inherent within all previous plagioclase-based hygrothermobarometer formulations (Putirka, 2008; Waters and Lange, 2015; Masotta and Mollo, 2019), introducing further uncertainties that are often not propagated. For the T and H_2O-dependent melt hygrothermobarometers, there are dedicated R scripts (Cutler, 2024) to perform error propagation (for either measured H_2O contents, independent T values, or calculated T/ H_2O estimates from melt-only models) or to generate predictions with T or H_2O values in a given range.

Application of the melt thermometers and hygrometers is suitable for a wide range of plagioclase-bearing melts across temperatures of 664–1355 °C and H_2O contents ≤11.20 wt.%; the melt barometer is only appropriate for pressures of ≤500 MPa. The plagioclase-saturated melt models were applied to melt inclusions and matrix glass from the 1980 Mount St Helens eruption and 2014-2015 Holuhraun eruption, with P-T-H_2O-An predictions returning consistent constraints comparable to estimates and observations from melt inclusion analyses, geophysical data, and previous hygrothermobarometric and plagioclase-equilibria models. The new set of models enables a quick assessment of plagioclase-melt equilibrium and an insight into the last-equilibrated P-T-H_2O conditions of plagioclase-bearing magmas in the upper crust.

Acknowledgements

We thank Caroline Martel, Gregor Weber, Duncan Muir, Christopher Firth, Annika Voigt, Bei Bei Morrison Evans, Felix Marxer and Matteo Masotta, who provided extra details on their experimental datasets or additional data. KSC acknowledges NERC studentship NE/S007474/1. JDB is supported by Royal Society Research Professorship (RP\R1\201048). Finally, we would like to thank Keith Putirka and Rebecca Lange for their constructive reviews.

Data Availability Statement

All experiments in the calibration datasets are listed in Table S1 and Table S3 but can also be accessed at https://doi.org/10.5281/zenodo.10841557. Figures were made with R Studio version 4.3.1 (available under the license AGPL version 3 or later: https://posit.co/downloads/) and edited in Affinity Designer 2. The R scripts (version 1.0) associated with this manuscript are licensed under MIT and preserved at https://doi.org/10.5281/zenodo.10841557. A user-friendly web app of the models can be found under the README section at https://github.com/kyra-cutler/Plag-saturated-melt-P-T-H2O-An. Updates to the models will also be available at https://github.com/kyra-cutler/Plag-saturated-melt-P-T-H2O-An.

References

Ágústsdóttir, T., Woods, J., Greenfield, T., Green, R. G., White, R. S., Winder, T., Brandsdóttir, B., Steinthórsson, S., & Soosalu, H. (2016). Strike-slip faulting during the 2014 Bárðarbunga-Holuhraun dike intrusion, central Iceland. *Geophysical Research Letters*, *43*(4), 1495-1503. DOI: https://doi.org/10.1002/2015GL067423

Ágústsdóttir, T., Winder, T., Woods, J., White, R. S., Greenfield, T., & Brandsdóttir, B. (2019). Intense seismicity during the 2014–2015 Bárðarbunga-Holuhraun rifting event, Iceland, reveals the nature of dike-induced earthquakes and caldera collapse mechanisms. *Journal of Geophysical Research: Solid Earth*, *124*(8), 8331-8357. DOI: https://doi.org/10.1029/2018JB016010

Andersen, D. J., & Lindsley, D. H. (1988). Internally consistent solution models for Fe-Mg-Mn-Ti oxides; Fe-Ti oxides. *American Mineralogist*, *73*(7-8), 714-726.

Bali, E., Hartley, M.E., Halldórsson, S.A., Gudfinnsson, G.H. and Jakobsson, S. (2018). Melt inclusion constraints on volatile systematics and degassing history of the 2014–2015 Holuhraun eruption, Iceland. *Contributions to Mineralogy and Petrology*, *173*, pp.1-21. DOI: 1 https://doi.org/0.1007/s00410-017-1434-1

Bamber, E.C., La Spina, G., Arzilli, F., de'Michieli Vitturi, M., Polacci, M., Hartley, M.E., Petrelli, M., Fellowes, J. and Burton, M. (2022). Basaltic Plinian eruptions at Las Sierras-Masaya volcano driven by cool storage of crystal-rich magmas. *Communications Earth & Environment*, *3*(1), p.253. DOI: https://doi.org/10.1038/s43247-022-00585-5

Berlo, K., Blundy, J., Turner, S. and Hawkesworth, C. (2007). Textural and chemical variation in plagioclase phenocrysts from the 1980 eruptions of Mount St. Helens, USA. *Contributions to Mineralogy and Petrology*, *154*, pp.291-308. DOI: https://doi.org/10.1007/s00410-007-0194-8

Blundy, J. (2022). Chemical differentiation by mineralogical buffering in crustal hot zones. *Journal of Petrology*, *63*(7), egac054. DOI: https://doi.org/10.1093/petrology/egac054

Blundy, J. and Cashman, K. (2005). Rapid decompression-driven crystallization recorded by melt inclusions from Mount St. Helens volcano. *Geology*, *33*(10), pp.793-796. DOI: https://doi.org/10.1130/G21668.1

Blundy, J., Cashman, K. and Humphreys, M. (2006). Magma heating by decompression-driven crystallization beneath andesite volcanoes. *Nature*, *443*(7107), pp.76-80. DOI: https://doi.org/10.1038/nature05100

Blundy, J., Cashman, K.V., Berlo, K., Sherrod, D.R., Scott, W.E. and Stauffer, P.H. (2008). Evolving magma storage conditions beneath Mount St. Helens inferred from chemical variations in melt inclusions from the 1980–1986 and current (2004–2006) eruptions. *US Geological Survey professional paper*, *1750*, pp.755-790.

Blundy, J., Cashman, K. V., Rust, A., & Witham, F. (2010). A case for CO2-rich arc magmas. *Earth and Planetary Science Letters*, *290*(3-4), 289-301. DOI: https://doi.org/10.1016/j.epsl.2009.12.013

Blundy, J. (2022). Chemical Differentiation by Mineralogical Buffering in Crustal Hot Zones. *Journal of Petrology*, *63*(7), egac054. DOI: https://doi.org/10.1093/petrology/egac054

Caricchi, L., Townsend, M., Rivalta, E. and Namiki, A. (2021). The build-up and triggers of volcanic eruptions. *Nature Reviews Earth & Environment*, *2*(7), pp.458-476. DOI: https://doi.org/10.1038/s43017-021-00174-8

Carlson, R.L. and Herrick, C.N. (1990). Densities and porosities in the oceanic crust and their variations with depth and age. *Journal of Geophysical Research: Solid Earth*, *95*(B6), pp.9153-9170. DOI: https://doi.org/10.1029/JB095iB06p09153

Cassidy, M., Manga, M., Cashman, K. and Bachmann, O. (2018). Controls on explosive-effusive volcanic eruption styles. *Nature communications*, *9*(1), p.2839. DOI: https://doi.org/10.1038/s41467-018-05293-3

Cassidy, M., Ebmeier, S. K., Helo, C., Watt, S. F. L., Caudron, C., Odell, A., ... & Castro, J. M. (2019). Explosive eruptions with little warning: Experimental petrology and volcano monitoring observations from the 2014 eruption of Kelud, Indonesia. *Geochemistry, Geophysics, Geosystems*, *20*(8), 4218-4247. DOI: https://doi.org/10.1029/2018GC008161

Cooper, C. L., Savov, I. P., & Swindles, G. T. (2019). Standard chemical-based tephra extraction methods significantly alter the geochemistry of volcanic glass shards. *Journal of Quaternary Science*, *34*(8), 697-707. DOI: https://doi.org/10.1002/jqs.3169

Cutler, K.S. (2024). kyra-cutler/Plag-saturated-melt-P-T-H2O-An: v1.0 (v1.0). *Zenodo.* DOI: https://doi.org/10.5281/zenodo.10841557

Devine, J. D., Gardner, J. E., Brack, H. P., Layne, G. D., & Rutherford, M. J. (1995). Comparison of microanalytical methods for estimating H2O contents of silicic volcanic glasses. *American Mineralogist*, *80*(3-4), 319-328. DOI: https://doi.org/10.2138/am-1995-3-413

Feig, S.T., Koepke, J. and Snow, J.E. (2010). Effect of oxygen fugacity and water on phase equilibria of a hydrous tholeiitic basalt. *Contributions to Mineralogy and Petrology*, *160*, pp.551-568. DOI: https://doi.org/10.1007/s00410-010-0493-3

Fuhrman, M. L., & Lindsley, D. H. (1988). Ternary-feldspar modeling and thermometry. *American mineralogist*, *73*(3-4), 201-215.

Gavrilenko, M., Krawczynski, M., Ruprecht, P., Li, W. and Catalano, J.G. (2019). The quench control of water estimates in convergent margin magmas. *American Mineralogist: Journal of Earth and Planetary Materials*, *104*(7), pp.936-948. DOI: https://doi.org/10.2138/am-2019-6735

Geiger, H., Mattsson, T., Deegan, F. M., Troll, V. R., Burchardt, S., Gudmundsson, Ó., Tryggvason, A., Krumbholz, M., & Harris, C. (2016). Magma plumbing for the 2014–2015 Holuhraun eruption, Iceland. *Geochemistry, Geophysics, Geosystems*, *17*(8), 2953-2968. DOI: https://doi.org/10.1002/2016GC006317

Ghiorso, M.S. and Gualda, G.A. (2015). An H 2 O–CO 2 mixed fluid saturation model compatible with rhyolite-MELTS. *Contributions to Mineralogy and Petrology*, *169*, pp.1-30. DOI: https://doi.org/10.1007/s00410-015-1141-8

Giordano, D., Russell, J.K. and Dingwell, D.B. (2008). Viscosity of magmatic liquids: a model. *Earth and Planetary Science Letters*, *271*(1-4), pp.123-134. DOI: https://doi.org/10.1016/j.epsl.2008.03.038

Giordano, G. and Caricchi, L. (2022). Determining the state of activity of transcrustal magmatic systems and their volcanoes. *Annual Review of Earth and Planetary Sciences*, *50*, pp.231-259. DOI: https://doi.org/10.1146/annurev-earth-032320-084733

Gualda, G.A. and Ghiorso, M.S. (2014). Phase-equilibrium geobarometers for silicic rocks based on rhyolite-MELTS. Part 1: Principles, procedures, and evaluation of the method. *Contributions to Mineralogy and Petrology*, *168*, pp.1-17. DOI: https://doi.org/10.1007/s00410-014-1033-3

Halldórsson, S.A., Bali, E., Hartley, M.E., Neave, D.A., Peate, D.W., Guðfinnsson, G.H., Bindeman, I., Whitehouse, M.J., Riishuus, M.S., Pedersen, G.B. and Jakobsson, S. (2018). Petrology and geochemistry of the 2014–2015 Holuhraun eruption, central Iceland: compositional and mineralogical characteristics, temporal variability and magma storage. *Contributions to Mineralogy and Petrology*, *173*, pp.1-25. DOI: https://doi.org/10.1007/s00410-018-1487-9

Hartley, M.E., Bali, E., Maclennan, J., Neave, D.A. and Halldórsson, S.A. (2018). Melt inclusion constraints on petrogenesis of the 2014–2015 Holuhraun eruption, Iceland. *Contributions to Mineralogy and Petrology*, *173*, pp.1-23. DOI: https://doi.org/10.1007/s00410-017-1435-0

Hayward, C. (2012). High spatial resolution electron probe microanalysis of tephras and melt inclusions without beam-induced chemical modification. *TheHolocene*, *22*(1), 119-125. DOI: https://doi.org/10.1177/0959683611409777

Helz, R.T. and Thornber, C.R. (1987). Geothermometry of Kilauea Iki lava lake, Hawaii. *Bulletin of volcanology*, *49*, pp.651-668. DOI: https://doi.org/10.1007/BF01080357

Higgins, O., Sheldrake, T. and Caricchi, L. (2022). Machine learning thermobarometry and chemometry using amphibole and clinopyroxene: a window into the roots of an arc volcano (Mount Liamuiga, Saint Kitts). *Contributions to Mineralogy and Petrology*, *177*(1), p.10. DOI: https://doi.org/10.1007/s00410-021-01874-6

Hilley, G. E. (ed.), Brodsky, E.E., Roman, D., Shillington, D. J., Brudzinski, M., Behn, M., Tobin, H. and the SZ4D RCN (2022). SZ4D Implementation Plan. Stanford Digital Repository.

Hirschmann, M. M., Ghiorso, M. S., Davis, F. A., Gordon, S. M., Mukherjee, S., Grove, T. L., M. Krawczynski, E. Medard, & Till, C. B. (2008). Library of Experimental Phase Relations (LEPR): A database and Web portal for experimental magmatic phase equilibria data. *Geochemistry, Geophysics, Geosystems*, *9*(3). DOI: https://doi.org/10.1029/2007GC001894

Housh, T.B. and Luhr, J.F. (1991). Plagioclase-melt equilibria in hydrous systems. *American Mineralogist*, *76*(3-4), pp.477-492.

Hughes, E. C., Buse, B., Kearns, S. L., Blundy, J. D., Kilgour, G., & Mader, H. M. (2019). Low analytical totals in EPMA of hydrous silicate glass due to sub-surface charging: Obtaining accurate volatiles by difference. *Chemical Geology*, *505*, 48-56. https://doi.org/10.1016/j.chemgeo.2018.11.015

Husen, A., Almeev, R.R. and Holtz, F. (2016). The effect of H2O and pressure on multiple saturation and liquid lines of descent in basalt from the Shatsky Rise. *Journal of Petrology*, *57*(2), pp.309-344. DOI: https://doi.org/10.1093/petrology/egw008

Iacovino, K., Matthews, S., Wieser, P.E., Moore, G.M. and Bégué, F. (2021). VESIcal Part I: An open-source thermodynamic model engine for mixed volatile (H2O-CO2) solubility in silicate melts. *Earth and Space Science*, *8*(11), p.e2020EA001584. DOI: https://doi.org/10.1029/2020EA001584

Jorgenson, C., Higgins, O., Petrelli, M., Bégué, F. and Caricchi, L. (2022). A Machine Learning-Based Approach to Clinopyroxene Thermobarometry: Model Optimization and Distribution for Use in Earth Sciences. *Journal of Geophysical Research: Solid Earth*, *127*(4), p.e2021JB022904. DOI: https://doi.org/10.1029/2021JB022904

Krawczynski, M.J., Grove, T.L. and Behrens, H. (2012). Amphibole stability in primitive arc magmas: effects of temperature, H2O content, and oxygen fugacity. *Contributions to Mineralogy and Petrology*, *164*(2), pp.317-339. DOI: https://doi.org/10.1007/s00410-012-0740-x

Kudo, A.M. and Weill, D.F. (1970). An igneous plagioclase thermometer. *Contributions to Mineralogy and Petrology*, *25*(1), pp.52-65. DOI: https://doi.org/10.1007/BF00383062

Kuhn, M. (2008). Building predictive models in R using the caret package. *Journal of statistical software*, *28*, pp.1-26. DOI: https://doi.org/10.18637/jss.v028.i05

Lange, R.A., Frey, H.M. and Hector, J. (2009). A thermodynamic model for the plagioclase-liquid hygrometer/thermometer. *American Mineralogist*, *94*(4), pp.494-506. DOI: https://doi.org/10.2138/am.2009.3011

Le Maitre, R.W., Bateman, P., Dudek, A. and Keller, J. (1989). Lameyre Le Bas. *MJ, Sabine, PA, Schmid, R., Sorensen, H., Streckeisen, A., Woolley, AR, Zanettin, B*, p.193.

Lees, J. M. (1992). The magma system of Mount St. Helens: Non-linear high-resolution P-wave tomography. *Journal of volcanology and geothermal research*, *53*(1-4), 103-116.

Li, X. and Zhang, C. (2022). Machine Learning Thermobarometry for Biotite-Bearing Magmas. *Journal of Geophysical Research: Solid Earth*, *127*(9), p.e2022JB024137. DOI: https://doi.org/10.1029/2022JB024137

Liu, E.J., Cashman, K.V., Miller, E., Moore, H., Edmonds, M., Kunz, B.E., Jenner, F. and Chigna, G. (2020). Petrologic monitoring at Volcán de Fuego, Guatemala. *Journal of Volcanology and Geothermal Research*, *405*, p.107044. DOI: https://doi.org/10.1016/j.jvolgeores.2020.107044

Longhi, J., Fram, M.S., Vander Auwera, J. and Montieth, J.N. (1993). Pressure effects, kinetics, and rheology of anorthositic and related magmas. *American Mineralogist*, *78*(9-10), pp.1016-1030.

Masotta, M. and Mollo, S. (2019). A new plagioclase-liquid hygrometer specific to trachytic systems. *Minerals*, *9*(6), p.375. DOI: https://doi.org/10.3390/min9060375

Namur, O., Charlier, B., Toplis, M.J. and Vander Auwera, J. (2012). Prediction of plagioclase-melt equilibria in anhydrous silicate melts at 1-atm. *Contributions to Mineralogy and Petrology*, *163*, pp.133-150. DOI: https://doi.org/10.1007/s00410-011-0662-z

Neave, D.A. and Putirka, K.D. (2017). A new clinopyroxene-liquid barometer, and implications for magma storage pressures under Icelandic rift zones. *American Mineralogist*, *102*(4), pp.777-794. DOI: https://doi.org/10.2138/am-2017-5968

Neave, D.A., Bali, E., Guðfinnsson, G.H., Halldórsson, S.A., Kahl, M., Schmidt, A.S. and Holtz, F. (2019). Clinopyroxene–liquid equilibria and geothermobarometry in natural and experimental tholeiites: the 2014–2015 Holuhraun eruption, Iceland. *Journal of Petrology*, *60*(8), pp.1653-1680. DOI: https://doi.org/10.1093/petrology/egz042

Neave, D.A. and Namur, O. (2022). Plagioclase archives of depleted melts in the oceanic crust. *Geology*, *50*(7), pp.848-852. DOI: https://doi.org/10.1130/G49840.1

Panjasawatwong, Y., Danyushevsky, L.V., Crawford, A.J. and Harris, K.L. (1995). An experimental study of the effects of melt composition on plagioclase-melt equilibria at 5 and 10 kbar: implications for the origin of magmatic high-An plagioclase. *Contributions to Mineralogy and Petrology*, *118*, pp.420-432. DOI: https://doi.org/10.1007/s004100050024

Papale, P., Moretti, R. and Barbato, D. (2006). The compositional dependence of the saturation surface of H2O+ CO2 fluids in silicate melts. *Chemical Geology*, *229*(1-3), pp.78-95. DOI: https://doi.org/10.1016/j.chemgeo.2006.01.013

Petrelli, M., Caricchi, L. and Perugini, D. (2020). Machine learning thermo-barometry: Application to clinopyroxene-bearing magmas. *Journal of Geophysical Research: Solid Earth*, *125*(9), p.e2020JB020130. DOI: https://doi.org/10.1029/2020JB020130

Pritchard, M.E., Mather, T.A., McNutt, S.R., Delgado, F.J. and Reath, K. (2019). Thoughts on the criteria to determine the origin of volcanic unrest as magmatic or non-magmatic. *Philosophical Transactions of the Royal Society A*, *377*(2139), p.20180008. DOI: https://doi.org/10.1098/rsta.2018.0008

Putirka, K.D. (2005). Igneous thermometers and barometers based on plagioclase+ liquid equilibria: Tests of some existing models and new calibrations. *American Mineralogist*, *90*(2-3), pp.336-346. DOI: https://doi.org/10.2138/am.2005.1449

Putirka, K.D. (2008). Thermometers and barometers for volcanic systems. *Reviews in mineralogy and geochemistry*, *69*(1), pp.61-120. DOI: https://doi.org/10.2138/rmg.2008.69.3

Putirka, K. (2016). Amphibole thermometers and barometers for igneous systems and some implications for eruption mechanisms of felsic magmas at arc volcanoes. *American Mineralogist*, *101*(4), pp.841-858. DOI: https://doi.org/10.2138/am-2016-5506

R Core Team, R. (2013). R: A language and environment for statistical computing.

Rutherford, M.J., Sigurdsson, H., Carey, S. and Davis, A. (1985). The May 18, 1980, eruption of Mount St. Helens: 1. Melt composition and experimental phase equilibria. *Journal of Geophysical Research: Solid Earth*, *90*(B4), pp.2929-2947. DOI: https://doi.org/10.1029/JB090iB04p02929

Saunders, K., Blundy, J., Dohmen, R. and Cashman, K. (2012). Linking petrology and seismology at an active volcano. *Science*, *336*(6084), pp.1023-1027. DOI: https://doi.org/10.1126/science.1220066

Scandone, R., & Malone, S. D. (1985). Magma supply, magma discharge and readjustment of the feeding system of Mount St. Helens during 1980. *Journal of Volcanology and Geothermal Research*, *23*(3-4), 239-262.

Sigmundsson, F., Hooper, A., Hreinsdóttir, S., Vogfjörd, K.S., Ófeigsson, B.G., Heimisson, E.R., Dumont, S., Parks, M., Spaans, K., Gudmundsson, G.B. and Drouin, V. (2015). Segmented lateral dyke growth in a rifting event at Bárðarbunga volcanic system, Iceland. *Nature*, *517*(7533), pp.191-195. DOI: https://doi.org/10.1038/nature14111

Spencer, K. J., & Lindsley, D. H. (1981). A solution model for coexisting iron–titanium oxides. *American mineralogist*, *66*(11-12), 1189-1201.

Stock, M.J., Bagnardi, M., Neave, D.A., Maclennan, J., Bernard, B., Buisman, I., Gleeson, M.L. and Geist, D. (2018). Integrated petrological and geophysical constraints on magma system architecture in the western Galápagos Archipelago: insights from Wolf volcano. *Geochemistry, Geophysics, Geosystems*, *19*(12), pp.4722-4743. DOI: https://doi.org/10.1029/2018GC007936

Thomson, A.R., Kohn, S.C., Prabhu, A. and Walter, M.J. (2021). Evaluating the formation pressure of diamond-hosted majoritic garnets: A machine learning majorite barometer. *Journal of Geophysical Research: Solid Earth*, *126*(3), p.e2020JB020604. DOI: https://doi.org/10.1029/2020JB020604

Ulmer, P., Kaegi, R. and Müntener, O. (2018). Experimentally derived intermediate to silica-rich arc magmas by fractional and equilibrium crystallization at 1· 0 GPa: an evaluation of phase relationships, compositions, liquid lines of descent and oxygen fugacity. *Journal of Petrology*, *59*(1), pp.11-58. DOI: https://doi.org/10.1093/petrology/egy017

Venezky, D.Y. and Rutherford, M.J. (1999). Petrology and Fe–Ti oxide reequilibration of the 1991 Mount Unzen mixed magma. *Journal of Volcanology and Geothermal Research*, *89*(1-4), pp.213-230. DOI: https://doi.org/10.1016/S0377-0273(98)00133-4

Waters, L.E. and Lange, R.A. (2015). An updated calibration of the plagioclase-liquid hygrometer-thermometer applicable to basalts through rhyolites. *American mineralogist*, *100*(10), pp.2172-2184. DOI: https://doi.org/10.2138/am-2015-5232

Weber, G., & Blundy, J. (2024). A machine learning-based thermobarometer for magmatic liquids. *Journal of Petrology*, egae020. DOI: https://doi.org/10.1093/petrology/egae020

Whitaker, M. L., Nekvasil, H., Lindsley, D. H., & Difrancesco, N. J. (2007). The role of pressure in producing compositional diversity in intraplate basaltic magmas. *Journal of Petrology*, *48*(2), 365-393. DOI: https://doi.org/10.1093/petrology/egl063

Wieser, P. E., Gleeson, M. L. M., Matthews, S., DeVitre, C. and Gazel, E. (2023a). Determining the Pressure –Temperature – Composition (P-T-X) conditions of magma storage. DOI: https://doi.org/10.31223/X50M44

Wieser, P., Kent, A.J. and Till, C., (2023b). Barometers behaving badly II: A critical evaluation of Cpx-only and Cpx-Liq thermobarometry in variably-hydrous arc magmas. *Journal of Petrology*, *64*(8), egad050. DOI: https://doi.org/10.1093/petrology/egad050

Wieser, P., Petrelli, M., Lubbers, J., Wieser, E., Ozaydin, S., Kent, A. and Till, C. (2023c). Thermobar: an open-source Python3 tool for thermobarometry and hygrometry. *Volcanica*, *5*(2), pp.349-384. DOI: https://doi.org/10.30909/vol.05.02.349384

Wieser, P.E., Kent, A.J., Till, C.B., Donovan, J., Neave, D.A., Blatter, D.L. and Krawczynski, M.J. (2023d). Barometers Behaving Badly I: Assessing the Influence of Analytical and Experimental Uncertainty on Clinopyroxene Thermobarometry Calculations at Crustal Conditions. *Journal of Petrology*, *64*(2), p.egac126. DOI: https://doi.org/10.1093/petrology/egac126

Wright, M. N., & Ziegler, A. (2017). ranger: A Fast Implementation of Random Forests for High Dimensional Data in C++ and R. *Journal of Statistical Software*, *77*(1), 1–17. DOI: https://doi.org/10.18637/jss.v077.i01

Yang, H.J., Kinzler, R.J. and Grove, T.L. (1996). Experiments and models of anhydrous, basaltic olivine-plagioclase-augite saturated melts from 0.001 to 10 kbar. *Contributions*

to Mineralogy and Petrology, *124*(1), pp.1-18. DOI: https://doi.org/10.1007/s004100050169

Yip, S.T.H., Biggs, J., Edmonds, M., Liggins, P. and Shorttle, O. (2022). Contrasting volcanic deformation in arc and ocean island settings due to exsolution of magmatic water. *Geochemistry, Geophysics, Geosystems*, *23*(7), p.e2022GC010387. DOI: https://doi.org/10.1029/2022GC010387

Zhang, Y., Xu, Z., Zhu, M. and Wang, H. (2007). Silicate melt properties and volcanic eruptions. *Reviews of Geophysics*, *45*(4). DOI: https://doi.org/10.1029/2006RG000216

Zimmer, M.M., Plank, T., Hauri, E.H., Yogodzinski, G.M., Stelling, P., Larsen, J., Singer, B., Jicha, B., Mandeville, C. and Nye, C.J. (2010). The role of water in generating the calc-alkaline trend: new volatile data for Aleutian magmas and a new tholeiitic index. *Journal of Petrology*, *51*(12), pp.2411-2444. DOI: https://doi.org/10.1093/petrology/egq062